HELLENIC REPUBLIC

National and Kapodistrian University of Athens

FACULTY OF GEOLOGY AND GEOENVIRONMENT

Department of Dynamic, Tectonic and Applied Geology

Study of the Katouna fault zone (western Greece): structural observations and geological mapping integrated with space based multitemporal SAR Interferometry

MSc Thesis

Varvara K. Tsironi

Supervisor:

Stylianos Lozios Ass. Professor

Konstantinos Soukis LTS

Athens 2017

HELLENIC REPUBLIC

National and Kapodistrian University of Athens

FACULTY OF GEOLOGY AND GEOENVIRONMENT
Department of Dynamic, Tectonic and Applied Geology

Study of the Katouna fault zone (western Greece): structural observations and geological mapping integrated with space based multitemporal SAR Interferometry

MSc Thesis

Varvara K. Tsironi

Examining Committee: Ass. Professor Stylianos Lozios (NKUA)

Professor Issaak Parcharidis (HUA)

Professor Efthymios Lekkas (NKUA)

To my mother for her patience,

Acknowledgments

From the moment, I started writing my Master Thesis, I was thinking about this chapter. This work was my Ithaka for a whole year. And as the poet Kavafis said,

Ithaka gave you the beautiful journey.

without her you wouldn't have set out

you should have already understood what Ithakas mean.

So, for this journey I would like to thank all the individuals who helped me to achieve my goals and they should be mentioned one by one.

First, I would like to thank Dr. Konstantinos Soukis and Prof. Stylianos Lozios who helped me to prepare my Master Thesis, as well as the help and support they have provided me for the duration of my postgraduate studies. I would like to thank Prof. Issaak Parcharidis who taught me the beautiful scientific field of SAR Interferometry and he inspired me to be passionate with my science. Also, I would like to say a great thank to Dr. Athanassios Ganas for the advices he has given me and for his constant attention in the scientific field that he provide me.

Also, I would like to thank individuals that helped me with their experience and knowledge, Konstantina Vlachou for all the advices she has given me in the GPS field. As well, I would like to thank the Remote Sensing Team of Harokopio University of Athens, and the geographer Asterios Papastergios. I would like to thank Pierre Briole, from Ecole Normale Superieure (ENS) Paris and Dr. Panagiotis Ilias, from National Observatory of Athens.

Furthermore, I would like to thank my friends. My best friends and colleagues, Theodora Kossiva, Stavroula Giannakopoulou and Christos Millas for their support, their advices and for believing in me. Also, I would like to thank my dear friend Athanasia-Maria Tompolidi who is my labmate, for the stimulating discussions and for the sleepless nights we were working together. Consequently, I would like to thank my friends especially, Panagiota Anninou for the assistance in the field and my beloved friend Odysseas Tarnaris who was standing next to me the whole time.

In the end, I would like to thank my family, who gave me the strength to go on and achieve my goal and especially, my mother and my father for believing in me and my brother for the many advices and the support.

Table of Images

Figure 1(a) Tectonic map of the Central and Eastern Mediterranean region with simplified plates model, modified from Chamot-Rooke et al. [2005]. South. Balk.: Southern Balkans; Alb.: Albania; Mac.: Macedonia; Bulg.: Bulgaria; Gre.: Greece; AP: Apulian platform; HP: Hyblean Plateau; KF: Kefalonia Fault; CR: Corinth Rift; TP: Thessaloniki Peninsula; NAT: North Aegean Trough. (b) Inset showing the nature of the crust in the region [Chamot-Rooke et al., 2005; Jolivet et al., 2008]. Black: Mesozoic remnant oceanic crust; dark gray: Neogene oceanic crust; light gray: Miocene post-orogenic thinned continental crust; white: continental crust; dashed line: accretionary prism over the crust.)Perouse et al.2016) 18

Figure 2 Geodynamic setting of Western Greece. Tectonic structures and crust nature are from Chamot-Rooke et al. (2005) and Papanikolaou et al. (2006). Velocity vectors, relative to fixed Eurasia, are from the regional interpolated velocity field (Perouse et al. 2012). AP: Apulian Platform; CR: Corinth Rift; CSZ: Calabrian Subduction Zone; KF: Kefalonia Fault; NAF: North Anatolian Fault; Pel: Peloponnesus. Black structures are active, gray ones are inactive (cf. Perouse et al.2012). The blue star is the rotation pole of the Apulian-Ionian microplate relative to the Nubian plate, shown with its 95 % confidence ellipse (Perouse et al. 2012). (Perouse et al., 2016) 20

Figure 3 Tectonic map of Western Greece from Perouse et al., 2016 showing active (red) and inactive (black) faults. 22

Figure 4 Neotectonic map of Amfilochia area modified after Katsavrias (1984a,b) and Papnikolaoy and Lekkas 1997. 28

Figure 5 Active and passive systems from Natural Resources Canada, 2016 32

Figure 6 Radar echo 36

Figure 7 SAR Imaging Geometry from DLR 38

Figure 8 An artistic expression of ERS-2 (http://www.esa.int/ESA) 40

Figure 9 An artistic impression of ENVISAT (http://www.esa.int/ESA) 43

Figure 10 A sinusoidal function sin ϕ is periodic with a 2π radian period. (http://www.esa.int/ESA) 46

Figure 11 Geometry in DinSAR (DLR) 51

Figure 12 Horizontal GPS velocity vectors relative to stable Eurasia from Chousianitis et al., 2015. Error ellipses represent 95 per cent confidence level. Abbreviations are as follows: NAT, North Aegean Trough; NAF, North Anatolian Fault; AT, Apulian Thrust; CTF, Cephalonia Transform Fault; MR, Mediterranean Ridge; HA, Hellenic Arc System; SCT, South Cretan Trough; PT, Pliny Trench; StT, Strabo Trench. 56

Figure 13 Model of the kinematics of the present-day crustal deformation in Central and Western Greece proposed from Chousianitis et al., 2015. Yellow colors correspond to rotation rates (numbers are degrees/Myr), blue colors to extension rates (numbers are ns/yr) and red colors to maximum shear strain rates (numbers are ns/yr). 58

Figure 14 Revised neotectonic map of Katouna area modified after Lekkas et al., 1997 61

Figure 15 Stereoplot (lower hemisphere projection) af the Katouna Fault Zone fault planes and associated slickensides. 62

Figure 16 Fault planes of KFZ with slickensides and tectonic clasts 65

Figure 17 Panoramic view of the Katouna Fault in the field 66

Figure 18. The fault scarp of the Katouna Fault 67

Figure 19 The display of Loutraki fault on map and the display of fault plane and slickenside in stereographic projection. 68

Figure 20 Loutraki fault surface in limestone and associated slickensides 69

Figure 21 Monastiraki Fault surface in Mesozoic limestones.....70

Figure 22 Horizontal GPS velocity vectors relative to stable Eurasia. The GPS data was provided from Chousianitis et al., 2015, Hollestein et al., 2008 and Vlachou 2006. ..72

Figure 23 Environment of Eoli-sa platform.....73

Figure 24 Multi-Interferometric Stacking Workflow 80

Figure 25 Singular Value Decomposition Workflow 81

Figure 26 Displacement map produced by Interferometric Stacking, from ascending ENVISAT ASAR images referring to 2002 to 2009 time span 86

Figure 27 Displacement map produced by Interferometric Stacking, from descending ENVISAT ASAR images referring to 2003 to 2010 time span 87

Figure 29 Synthetic map of InSAR result and geological data. Displacement map produced by Interferometric Stacking, from ascending ENVISAT ASAR images referring to 2002 to 2009 time span.....88

Figure 28 Synthetic map of InSAR result and geological data. Displacement map produced by Interferometric Stacking, from descending ENVISAT ASAR images referring to 2003 to 2010 time span.....89

Figure 30 Stacking LOS displacement rate obtained from ascending ENVISAT ASAR images referring to 2002 to 2009 with the main tectonic structures of the area. Section is shown as black line along with their corresponding surface diagrams. 90

Figure 31 Stacking LOS displacement rate obtained from descending ENVISAT ASAR images referring to 2003 to 2010 with the main tectonic structures of the area. Section is shown as black line along with their corresponding surface diagrams. 91

Figure 32 SVD displacement rate from ascending ENVISAT ASAR images referring to 2002 to 2009 time span 92

Figure 33 SVD displacement rate from descending ENVISAT ASAR images referring to 2003 to 2010 time span 93

Figure 34 The KFZ as a transfer fault between to grabens 95

Figure 35 The evidences of left-lateral movement between the two blocks.....96

Figure 36 Stacking LOS displacement rate obtained from ascending ENVISAT ASAR images referring to 2002 to 2009 with the main tectonic structures of the area. Section is shown as black line along with their corresponding surface diagrams. Also, in the graph it is located the boundary of evaporite layer. 99

Figure 37 Stacking LOS displacement rate obtained from descending ENVISAT ASAR images referring to 2003 to 2010 with the main tectonic structures of the area. Section is shown as black line along with their corresponding surface diagrams. Also, in the graph it is located the boundary of evaporite layer. 100

Table of Contents

Acknowledgments 3

Table of Images 4

Abstract 10

Περίληψη 12

Introduction 14

Geological Settings 17

Hellenic Arc 18

Geodynamics in Western Greece 21

Previous studies 24

Tectonostratigraphy 27

Earth Observation System, SAR Interferometry and GPS 31

SAR Sensors 33

Synthetic Aperture Radar (SAR) 36

ERS Satellite 39

Envisat Satellite 41

Synthetic Aperture Radar (SAR) Interferometry 44

Basic Principles 45

Differential SAR interferometry (DInSAR) 50

GPS Operation System 52

GLONASS 54

GPS Studies and Strain Analysis 55

Geological Data 59

Katouna Fault Zone 62

Loutraki Fault 68

Monastiraki Fault 70

GPS Data 71

SAR Processing and Results 73

EOLi Platform - Datasets 73

Software and Processing 77

GAMMA Remote Sensing Software 77

SAR Processing 78

Results 86

Discussion 94

Conclusions 102

References 104

Abstract

The termination of the Hellenic subduction zone is located in Western Greece and coincides with the Kefallinia dextral strike slip fault zone. Further east, in western mainland Greece, normal and strike-slip faulting coexist. The Katouna Fault Zone is a major NNW-SE fault zone that connects the extensional half-graben of Amvrakikos Gulf to the extensional graben of Patras Gulf. In order to study the Katouna Fault Zone we combined geological mapping, structural observations, remote sensing, GPS and data.

Detailed geological mapping revealed that the Katouna Fault zone is hosted in the mid-Triassic strongly brecciated evaporate layer, which is the basal layer of the Ionian zone. The fault zone comprises several NNW-SSE discrete fault surfaces flanking the evaporites. On these surfaces, we identified and measured strike-slip slickenlines. Numerous kinematic indicators (grooves, clasts, small-scale corrugations), indicate left-lateral slip along the fault zone.

Further study of the differential movement across KFZ has been achieved using the state of the art technology of Synthetic Aperture Radar (SAR) interferometry through time-series analysis. A Singular Value Decomposition (SVD) interferometric analysis was applied using descending and ascending datasets of ENVISAT ASAR SLC images and the interferometric stacking, in order to investigate the ground motion rate. The derived displacement maps showed a differential movement across the fault zone, as revealed by their different acquisition geometries. This indicates that the horizontal component of displacement is much more significant than the vertical component. Interestingly, the transition from areas with negative to areas with positive displacements is not a discrete line but a few kilometers wide zone, which more or less coincides with the mid-Triassic evaporite layer. Published GPS vectors in general, show a SW motion but the western block velocities are higher compared to the eastern block.

Based on the above evidence, we conclude that the Katouna Fault Zone is a major active left-lateral strike slip fault zone which transfers the movement between the extensional half-graben of Amvrakikos Gulf to the extensional graben of Patras Gulf.

Περίληψη

Η μετάβαση από τη ζώνη υποβύθισης στο Ελληνικό τόξο στη ζώνη σύγκρουσης των πλακών της Απουλίας και της Ευρασιατικής εδρεύει στη Δυτική Ελλάδα και συμπίπτει με το δεξιόστροφο ρήγμα οριζόντιας ολίσθησης της Κεφαλλονιάς. Ανατολικότερα αυτής της μετάβασης, στη δυτική ηπειρωτική Ελλάδα, συνυπάρχουν εφελκυστικού τύπου κανονικά ρήγματα και οριζόντιας ολίσθησης ρήγματα. Η ρηξιγενής ζώνη της Κατούνας είναι μια σημαντική ρηξιγενής ζώνη με διεύθυνση NNW-SE που συνδέει την ημιτάφρου του Αμβρακικού Κόλπου με την τάφρου του Πατραϊκού Κόλπου. Για να μελετήσουμε τη ζώνη αυτή συνδυάσαμε τη γεωλογική χαρτογράφηση και τις παρατηρήσεις υπαίθρου, εφαρμογές της Τηλεπισκόπησης και μετρήσεις GPS.

Η λεπτομερής γεωλογική χαρτογράφηση αποκάλυψε ότι η ρηξιγενής ζώνη της Κατούνας φιλοξενείται στο Τριαδικό εβαποριτικού στρώμα, το οποίο είναι ο κατώτερος στρωματογραφικός σχηματισμός της Ιόνιας γεωτεκτονικής ενότητας . Η ρηξιγενής ζώνη περιλαμβάνει αρκετές διακριτές επιφάνειες ολίσθησης με διεύθυνση NNW-SSE μέσα στον εβαπορίτη. Σε αυτές τις επιφάνειες, εντοπίσαμε και μετρήσαμε γραμμές ολίσθησης που υποδεικνύουν την κινηματική του ρήγματος. Πολυάριθμοι κινηματικοί δείκτες (αυλακώσεις, γραμμές ολίσθησης, τεκτονικοί κλάστες) υποδηλώνουν τη σημαντική οριζόντια συνιστώσα της κίνησης κατά μήκος της ρηξιγενής ζώνης.

Περαιτέρω μελέτη της διαφορικής κίνησης κατά μήκος του ρήγματος έχει επιτευχθεί με τη χρήση της τελευταίας τεχνολογίας, της Διαφορικής Συμβολομετρίας Ραντάρ Συνθετικού Ανοίγματος (DInSAR) μέσω ανάλυσης χρονοσειρών. Για τη διερεύνηση του ρυθμού παραμόρφωσης εφαρμόστηκε η συμβολομετρική τεχνική της ενιαίας τιμής SVD (Singular Value Decomposition Value) με χρήση ανοδικής και καθοδικής τροχιάς δεδομένων των εικόνων ENVISAT ASAR SLC καθώς και η τεχνική της σώρευσης συμβολογραφημάτων. Οι χάρτες

παραμορφώσεων που προέκυψαν έδειξαν διαφορική κίνηση στη ρηξιγενή ζώνη, όπως αποκαλύπτεται από τις διαφορετικές γεωμετρίες των εικόνων λήψης. Αυτό υποδεικνύει ότι η οριζόντια συνιστώσα της μετατόπισης επικρατεί σε σχέση με την κατακόρυφη συνιστώσα της κίνησης. Είναι ενδιαφέρον ότι η μετάβαση από περιοχές με αρνητικές σε περιοχές με θετικές μετατοπίσεις δεν είναι μια διακεκριμένη γραμμή αλλά μια ζώνη πλάτους λίγων χιλιομέτρων, η οποία συμπίπτει με τα όρια του εβαποριτικού στρώματος. Οι μετρήσεις GPS από βιβλιογραφικά δεδομένα γενικά δείχνουν κίνηση προς τα SW αλλά οι ταχύτητες δυτικού μπλοκ είναι μεγαλύτερες και σχεδόν διπλάσιες σε σύγκριση με το ανατολικό μπλοκ.

Με βάση τα παραπάνω στοιχεία, καταλήγουμε στο συμπέρασμα ότι η ρηξιγενής ζώνη της Κατούνας είναι Katouna είναι μια σημαντική ενεργή αριστερόστροφη οριζόντιας ολίσθησης δομή, η οποία μεταφέρει την κίνηση μεταξύ της ημι-τάφρου του Αμβρακικού Κόλπου και της τάφρου του Πατραϊκού Κόλπου του κόλπου της Πάτρας.

Introduction

Western Greece, an area consisting of two main tectonic structures, namely the Cephalonia fault and the Katouna fault zone. The study area is located internally to the western part of the Hellenic Arc and Trench System, which is the result of the Hellenic subduction. Its origin is linked to the northward motion of the African plate (McKenzie, 1972).

In the northwest trending part of Hellenic arc, there are two segments. The first presents slow subduction rate while the second, fast subduction rate. The northern and southern segments of the Hellenic subduction boundary are separated by the dextral Cephalonia fault (Royden and Papanikolaou, 2011).

The Cephalonia Transform Fault accommodates the relative motion between the Apulia and the Eurasia lithospheric plates (Valkaniotis et al., 2014). This transform system is kinematically linked to the shortening across the southern Hellenic trench and the dextral shear in the mainland Greece (Kahle et al., 1995).

In the mainland, there is a "fold and thrust" system along the western edge of continental Greece and a fault zone in the East, controlled by extensional tectonism (Doutsos et al., 1987). This system, is considered as inactive.

Furthermore, the most recent structures that can be detected in the region could indicate a connection between the right-slip Cephalonia fault zone and the extension in the Amvrakikos Gulf and, hence, to the left-slip fault zone along the Katouna-Stamna area (Brooks et al., 1988, Clews et al., 1989).

Previous tectonic studies in the area indicate an active fault network, which is composed by the E-W striking extensional systems (grabens), which are connected by a NW-striking left lateral fault zone (Melis and Burton, 1988, Clews, 1989, Mercier et al., 1989, Underhill, 1989). The active left-lateral fault zone, called Amvrakia or Katouna fault (Haslinger et al., 1999), does not show clear geological and

geomorphological evidence. The block in Akarnania bounded to the north by Amvrakikos Gulf (tectonic graben), to the west by the Cephalonia transform fault and to the east by Katouna-Stamna fault zone which is a NW-striking left-lateral system crossing from Gulf of Amvrakikos to Patras-Corinth rift

On the other hand, Radar interferometry (Gabriel et al., 1989; Massonnet and Feigl, 1998; Hanssen, 2001) is based on the use of phase information that is obtained by Synthetic Aperture Radar (SAR). SAR interferometry is an effective technique to map elevation as well as elevation changes with differential interferometry (DInSAR). Additionally, millimetric target displacement along the line of sight (LOS) directions can be detected allowing the measurement of slow terrain motion (Ferretti et al., 2001). Using large stacks of SAR images acquired over the same area, long deformation time series can be analyzed using multi-temporal differential SAR interferometry techniques.

In the current study, the monitoring and mapping of the ground motion, which is occurring in the broader region of Katouna, is based on the application of a multi-temporal interferometric stacking technique and hybrid multi-temporal radar interferometry technique using SVD algorithm (combining DInSAR, PSI and SBAS properties) (Wasowski & Bovenga, 2014).

The main targets of the Thesis are to establish the strike slip character of Katouna fault zone based on hard kinematic evidence e.g. the presence of sub-horizontal slickensides and to try to identify the differential movement across the fault through mapping the potential land motion over the broader area of the Katouna, producing multi-temporal interferometric displacement maps using two ENVISAT datasets of SAR scenes spanning the period 2002-2009 and 2003-2010 in descending and ascending acquisition geometry, and two ERS datasets of SAR scenes spanning the period 1995-1999 in descending and ascending acquisition geometry. Also, the construction of a map with GPS vectors which indicate the movement in the horizontal level. In order to combine the geological observations with the InSAR

results, the production of synthetic maps which interpret how the geological formations link with the ground motion and the fault movement, took place.

Geological Settings

The studied area is located in western Greece and it belongs to the geodynamic regime of the Mediterranean Sea. The present tectonic evolution is the result of the progressive closure of the space between the two plates, the converging African and the Eurasian plate. This tectonic pattern is very complex and consists of the evolving Maghrebian margin to the west, the ultra-slow Calabrian subduction in the central part and the rapid subduction in the Hellenic trench (Perouse et al., 2012).

The tectonic evolution of Eastern Mediterranean, has been controlled by the collapse of the Alpine orogenic belt. Based mainly on geologically and geophysical observations, various kinematic models for the area of the Eastern Mediterranean have been developed (McKenzie, 1972,1978, Le Pichon & Angelier, 1979, Mc Kenzie & Jackson, 1983). In details, the Alpine orogenic belt was created from the closure of the Tethyan deep marine and/or oceanic basins and the subsequent collision of the Apulian continent against the Eurasia. The opening of the Ionian Sea was the main reason for the separation of the Apulian continent from the African margin in Early Jurassic (Rosenbaum et al., 2004). On the other hand, the collapse of the Alpine belt in the Mediterranean region followed in the late Oligocene to Miocene times (Rosenbaum et al., 2004). From the late Miocene to recent the present-day configuration gradually formed.

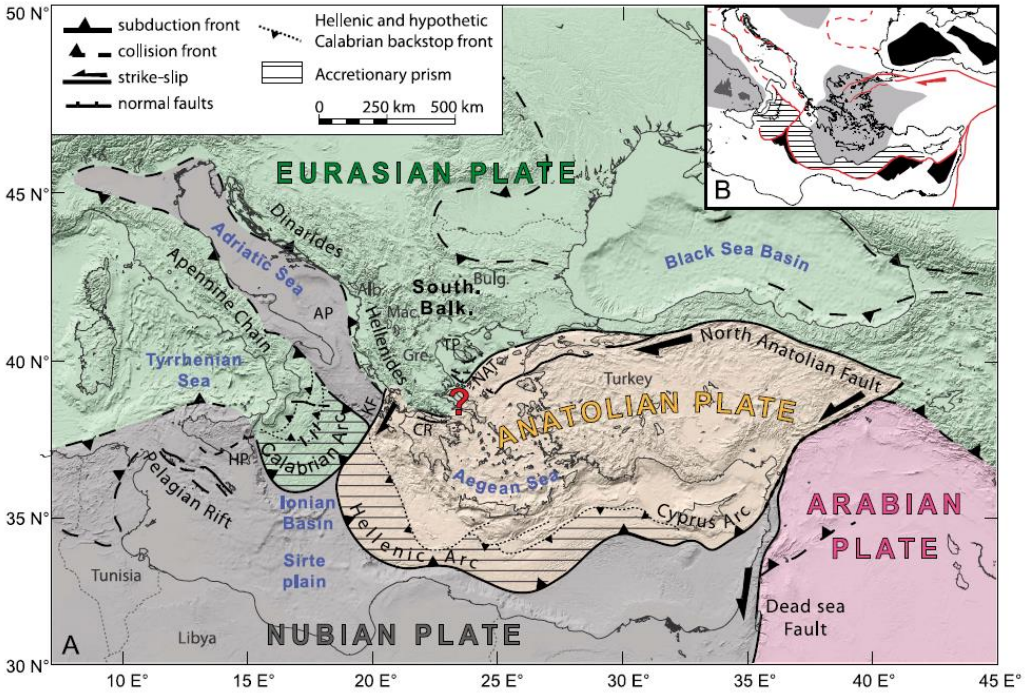

Figure 1(a) Tectonic map of the Central and Eastern Mediterranean region with simplified plates model, modified from Chamot-Rooke et al. [2005]. South. Balk.: Southern Balkans; Alb.: Albania; Mac.: Macedonia; Bulg.: Bulgaria; Gre.: Greece; AP: Apulian platform; HP: Hyblean Plateau; KF: Kefalonia Fault; CR: Corinth Rift; TP: Thessaloniki Peninsula; NAT: North Aegean Trough. (b) Inset showing the nature of the crust in the region [Chamot-Rooke et al., 2005; Jolivet et al., 2008]. Black: Mesozoic remnant oceanic crust; dark gray: Neogene oceanic crust; light gray: Miocene post-orogenic thinned continental crust; white: continental crust; dashed line: accretionary prism over the crust.)Perouse et al.2016)

Hellenic Arc

The importance of the Hellenic arc as part of the Alpine -Himalayan orogeny was recognized very early (McKenzie, 1972). It is the result of the Hellenic subduction and its origin is linked to the northward motion of the African plate. The Hellenic Arc stretches, from Scutari-Pec (NW), in the central-south Adriatic Sea to the Gulf of Antalya eastwards in the western Anatolia, with a total length of approximately 1500km (McKenzie, 1978, Le Pichon & Angelier, 1979, Picha, 2002, Reilinger et al., 2006). The Consequently, its trend is NNW-SSE in mainland Greece, gradually turns to E-W from Kithira and Crete and concludes in a NE-SW trend in the Dodecanese Islands and Lycia of Asia Minor into the Isparta and Antalya.

In the early Miocene to Late Miocene the gravitational collapse of the crust took place as a response to the retreat of the Hellenic slab. This was accompanied by the consumption of the remnant Mesozoic Ionian Sea oceanic crust, and the back-arc extension in the Aegean Sea. In the Aegean Sea, the development of low-angle detachment faults was active during this period (Jolivet and Brun, 2010). The extensional detachment systems, that are correlated with the back-arc extension, extends further to the North until the central Bulgaria with E-W trending grabens (Burchfiel et al., 2000). From GPS data accrue indications that the convergence rate is about 5-10mm/y across the northern Aegean (Hollenstein et al., 2008, Bennett et al., 2008, Vassilakis et al., 2011) and about 35mm/y across southern part of the Hellenides. The continued convergence in the whole area of the arc is confirmed by the seismic activity with reverse focal mechanisms for the local earthquakes in large depths (e.g., Louvari et al., 1999, Papazachos et al., 2000).

During the Late Miocene-Early Pliocene the collision of the Apulian plate to Albania and western Greece took place. The continuing subduction led to the creation of the dextral Cephalonia fault, to balance the transition between the continental collision in northwestern Greece and the oceanic subduction below Peloponnese.

According to Royden and Papanikolaou (2011), in the northwest trending part of Hellenic arc, there are two segments. The first one presents low subduction rate while the second, rapid subduction rate. The northern and southern segments of the Hellenic subduction boundary are separated by the dextral Cephalonia fault. GPS data indicate dextral motion and a displacement rate of about 25mm/y (Royden and Papanikolaou, 2011). Moreover, the crust of the lithosphere below the Peloponnesus is particularly thin, about 8km, however, the crustal thickness increases to 20km in the area around the Cephalonia fault zone (Pearce et al.,2012).

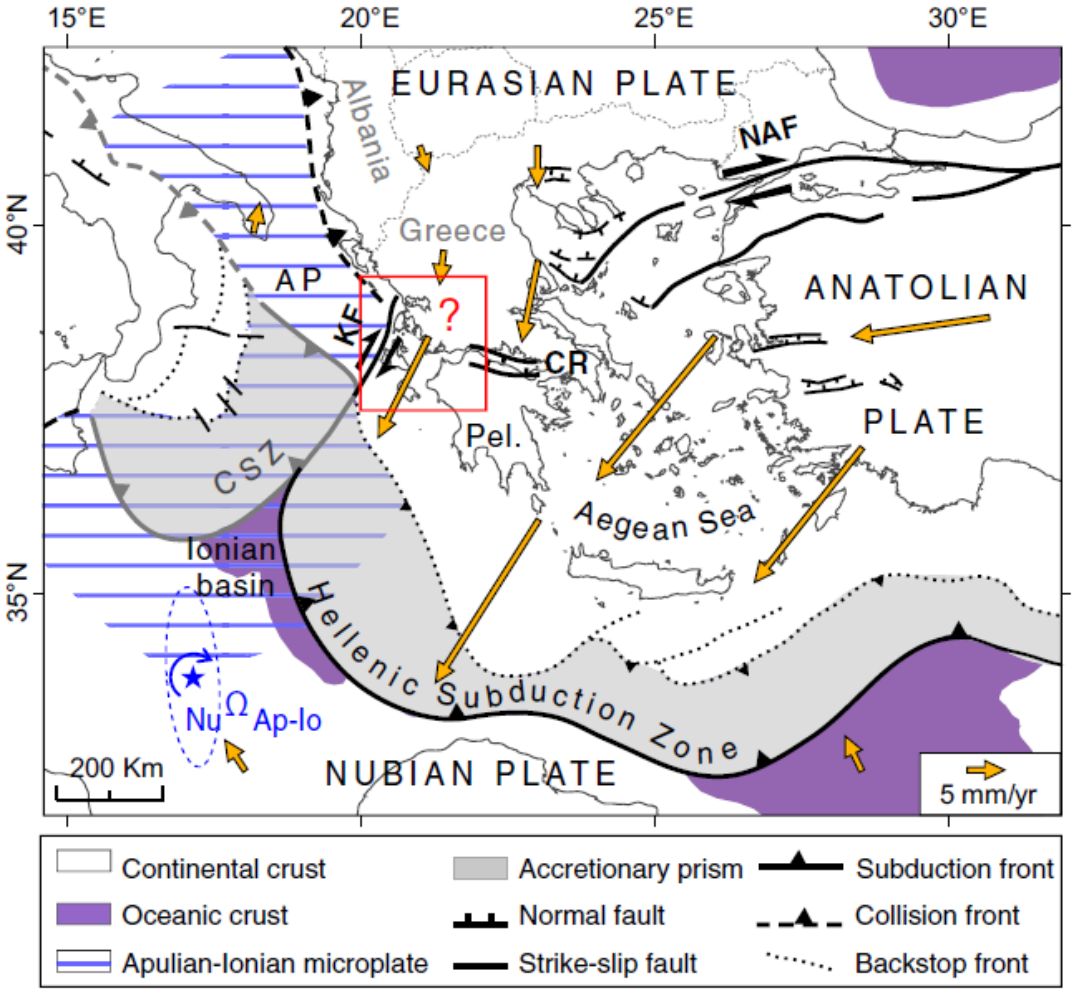

Figure 2 Geodynamic setting of Western Greece. Tectonic structures and crust nature are from Chamot-Rooke et al. (2005) and Papanikolaou et al. (2006). Velocity vectors, relative to fixed Eurasia, are from the regional interpolated velocity field (Perouse et al. 2012). AP: Apulian Platform; CR: Corinth Rift; CSZ: Calabrian Subduction Zone; KF: Kefalonia Fault; NAF: North Anatolian Fault; Pel: Peloponnesus. Black structures are active, gray ones are inactive (cf. Perouse et al.2012). The blue star is the rotation pole of the Apulian-Ionian microplate relative to the Nubian plate, shown with its 95 % confidence ellipse (Perouse et al. 2012). (Perouse et al., 2016)

Geodynamics in Western Greece

As mentioned earlier, the studied area is located in western Greece, an area consisting of two main tectonic structures, namely the Cephalonia fault and the Katouna fault zone. The Cephalonia Transform Fault is an offshore right-lateral strike-slip fault. The length of the zone is about 100km long and accommodates the relative motion between the Apulia and the Eurasia lithospheric plates (Valkaniotis et al., 2014). Cephalonia Fault is separated in two segments, the Lefkada segment and the Cephalonia segment. The first one can be identified offshore northern Cephalonia Island and strikes in a NNW-SSE direction with a length of about 40km. The second segment starts immediately after the first and has approximately 60km length (Louvari et al., 1998). These two major fault segments, with the addition of some other minor faults in the Ionian Islands, form the Cephalonia Transform Fault Zone, which connects the thrust belt along the Hellenic arc in the South to the one along the northwestern Greece and western Albania in the North (Louvari et al., 1998).

This transform system is kinematically linked to the shortening across the southern Hellenic trench and the dextral shear in the mainland Greece (Kahle et al., 1995). A problem concerning this particular fault is that no evidence of any deformation has been discovered onshore yet however, in western Greece, there is a "fold and thrust" system along the western edge of continental Greece and a fault zone in the East, controlled by extensional tectonism (Doutsos et al., 1987). That "fault and thrust" system is not active in the present, because some new structures were formed, as a result of extension, that overprinted the older structures. Such normal and strike-slip faults that overprinted older thrusts and reverse faults can be found in western Greece.

The tectonic evolution of these older structures is more apparent in the northwest continental Greece. In example, the basins of Paleros and Mytikas were created by this "fault and thrust" system. In further detail, the eastern part of the

Paleros basin dates to the Late Miocene period, while the western part of the basin is post-Miocene. Additionally, the Pliocene sediments are thicker at the, nearby, Pogonia village than the Paleros region. Such findings could potentially indicate a westward migration of subsidence at that time. These two basins were tectonically active until the Pliocene-Pleistocene boundary (Doutsos et al., 1987).

Furthermore, the newest structures that can be detected in the region could

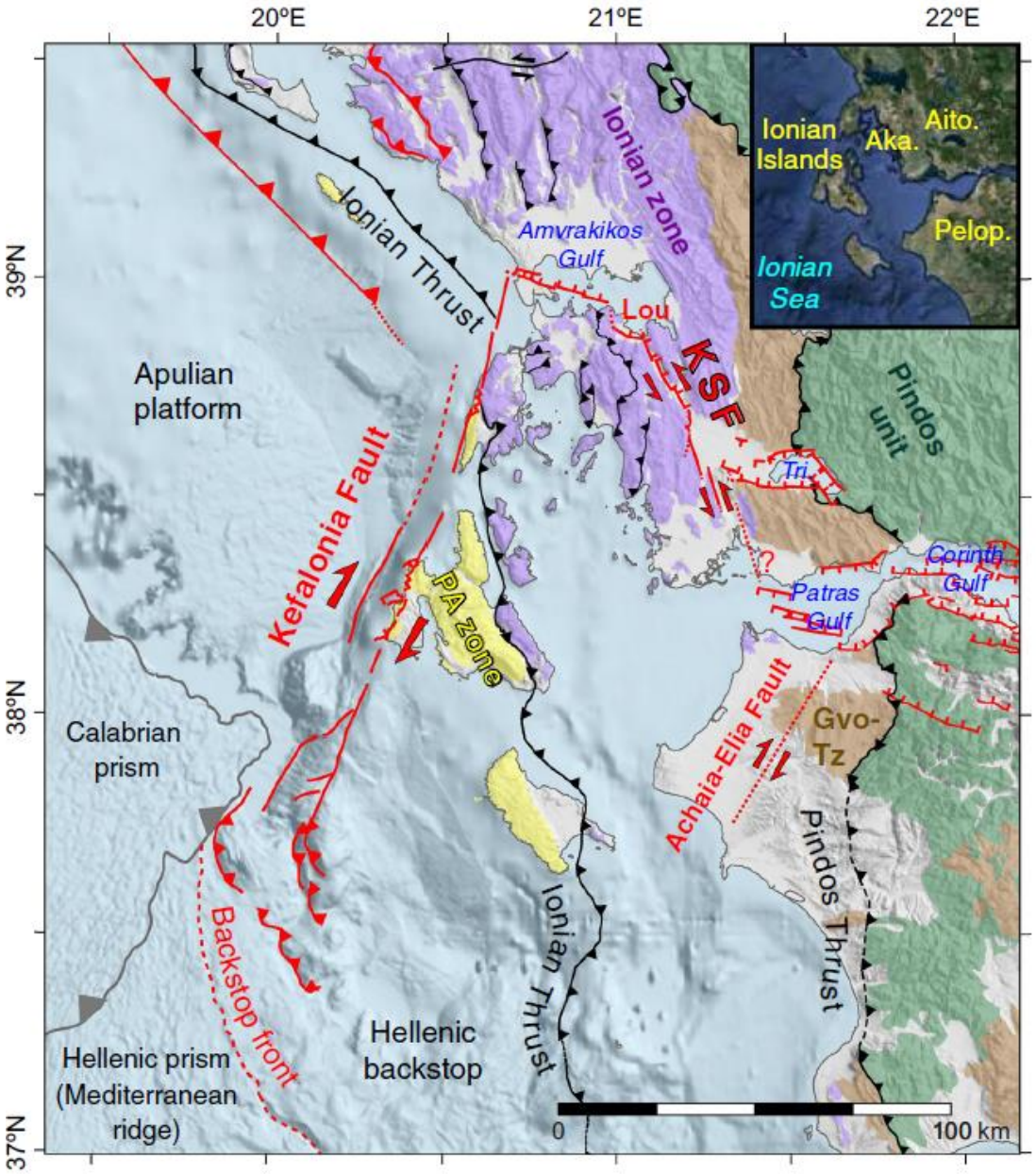

Figure 3 Tectonic map of Western Greece from Perouse et al., 2016 showing active (red) and inactive (black) faults.

indicate a connection between the right-slip Cephalonia fault zone and the extension in the Amvrakikos Gulf and, hence, to the left-slip fault zone along the Katouna-Stamna area (Brooks et al., 1988, Clews et al., 1989). All the above constitute tectonic implications of the lateral transition in the overriding plate from oceanic to continental collision (Perouse et al., 2016). In the mainland, the NNW-striking Hellenides units and the Neogene "fault and thrust" system are overprinted by E-W-striking extensional systems, such as the Trichonis Lake and the Gulf of Amvrakikos, Corinth Patras. According to (Jolivet et al., 2010) the cause of these phenomena is the retreat of the slab. In this part of Greece the extension process is estimated to have started during the Pliocene. In the Gulf of Corinth, the fault activity migrated to the north resulting in the dipping faults of the present-day southern Gulf of Corinth (Ford et al., 2013, Jolivet et al., 2010). This extensional system, possibly, correlates with the strike-slip structures in western Greece, and is located between the grabens of the two Gulfs of Amvrakikos and Corinth.

Previous studies

Previous studies indicate an active fault network composed by the E-W striking extensional systems (grabens), which are connected by a NW-striking left lateral fault zone (Melis and Burton, 1988, Clews, 1989, Mercier et al., 1989, Underhill, 1989). No clear geological and geomorphological evidences were reported for the active left-lateral fault zone, called Amvrakia or Katouna fault (Haslinger et al., 1999), until Vassilakis et al., 2011 observed within the Mesozoic limestones and Perouse et al., 2016 found morphotectonic evidences in Katouna valley and slickensides which are an evidence of the horizontal component for the slip of the fault zone.

Many research groups proposed the existence of a block in Akarnania bounded to the north by Gulf of Amvrakikos (tectonic graben), to the west by the Cephalonia transform fault and to the east by Katouna-Stamna fault zone, which is a NW-striking left-lateral system crossing from Gulf of Amvrakikos to Patras-Corinth rift (Le Pichon et al., 1995, Konstantinou et al., 2009, Cocard et al., 1999, Hollestein et al., 2008). Vassilakis et al., 2011 proposed another model indicating that the extension transfer from gulf of Amvrakikos to Gulf of Corinth- Patra was accomplished through the Trichonis lake graben and a left-lateral fault in Amphilochia valley. In this paper, the above block called Akarnania segment, which has internal deformation within the fragment by reactivation of the N-striking Neogene Hellenic thrusts as present-day normal faulting.

On the other hand, Perouse et al., 2016 proposed the Ionian Islands-Akarnania block (IAB) which shares several similarities with the Akarnania fragment by Vassilakis et al., 2011. However, they propose that the eastern boundary is the left-lateral fault Katouna fault, indicating the southern Katouna Stamna fault (KSF) connects directly with the Gulf of Patras and proposed that the Trichonis graben, located at the junction between Katouna and the Stamna faults, accommodates the

left-lateral slip rate difference between the northern (~11mm) and southern(~6mm) Katouna-Stamna fault.

According to Vassilakis et al., 2011, the young and active deformation in western Greece is represented by a network of extensional basins and strike-slip faults that connect the extensional domains. They propose the existence of triple junction-like structures, the first is located near the western end of Gulf of Corinth, at the junction between Karpenissi, Akarnania and Northwest Peloponnese fragments. These fragments are distinguished based on differences between the GPS velocities. The second is located near Amvrakikos half-graben where the junction occurs between the Cephalonia transform fault, the convergent zone of external Hellenides and the left-lateral Amphilochia fault zone. In addition, the interconnected network of young deformation zones outlined the transfer of the extension within the gulf of Corinth to the compressive structures along the Hellenic trench. This network is constituted by crustal fragments with active internal deformation, bounded by zones in which the active faulting localized, such as the Amphilochia fault zone.

On the other hand, Perouse et al., 2016 proposed the left-lateral Katouna-Stamna Fault (KSF), a 65km NNW-striking fault system connecting the Amvrakikos to Patras Gulf. KSF is interpreted as a newformed immature fault system, which is likely controlled by the Hellenides orogen, and forms the northeastern boundary of IAB. This fault zone is separated to northern and southern part. The northern part, e.g. the Katouna segment, has left-lateral slip rate 11mm/y, and the southern part, e.g. the Stamna segment, has 6mm/y left-lateral slip rate, according to GPS data. KSF slip rate is high because the CRE dating indicated slip rate of 4mm/y on the Katouna valley segment. Perouse et al.2016 suggested that the fault has an aseismic creeping behavior due to the localized strain and high slip rate, the gypsum-breccias bedrock and the low seismicity. Also, they proposed the IAB has no internal deformation because the Hellenides thrusts are no longer active, based on either field

observations and GPS data. Finally, the IAB became progressively individual from Pleistocene (younger than ~1.5Ma) to the present day, due to a change from E-W compressional regime to near N-S extensional stress regime.

Another study from University of Patras had taken place in the broader area of the case study. Gkardi, 2011 proposed two main segments of the left-lateral fault zone, the Katouna fault and Amphilochia fault, and they applied a morphotectonic analysis along the NNW-trending fault zones of Katouna and Amphilochia. Several morphotectonic indices were implemented. The presence of long and asymmetric basins on the footwall block of the fault zones and the associated seismicity along them confirms that the segments are tectonically active. The fault zones of Katouna and Amphilochia appear to be characterized by an intermediate type of deformation, showing extensional deformation in a NE-orientation and sinistral shear deformation along their NNW-orientation. The Katouna and Amphilochia fault zones appears to act as a composite transfer zone accommodating left-lateral oblique extension between the more active WNW-directed grabens of Amvrakikos and Gulf of Patras (Gkardi, 2011).

Tectonostratigraphy

The geological structure of Greece consists of Variscan pre-alpine rocks and Mesozoic to Cenozoic alpine formations. The alpine rocks were deposited in shallow and deep marine to oceanic basins, belonging to the Tethys Ocean that separated Gondwanan from Eurasia (Papanikolaou, 2013). When the Tethys Ocean started closing in mid Jurassic all these units started to accrete to the southern European margin. As a result, most of these units were intensely deformed with folding and thrusting and some of them were metamorphosed under HO/LT conditions, often followed by greenschists to amphibolite facies metamorphism.

The tectonostratigraphy of the studied area was defined based on the the geological map of "Amphilochia sheet"," Vonitsa sheet", created in 1984 by Katsavrias, and the neotectonic map of Aitoloakarnania, created in 1997 by Lekkas and Papanikolaou, and field observations. It consists of alpine formations of the Ionian Unit (Papanikolaou 2015), and Plio-Pleistocene and Quantenary sediments.

The alpine rocks that are exposed in the studied area are part of the Ionian unit. The stratigraphic column of Ionian unit begins with the Triassic evaporites, mostly consisting black-grey gypsum and anhydrites (Vassilakis et al.,2011). In many

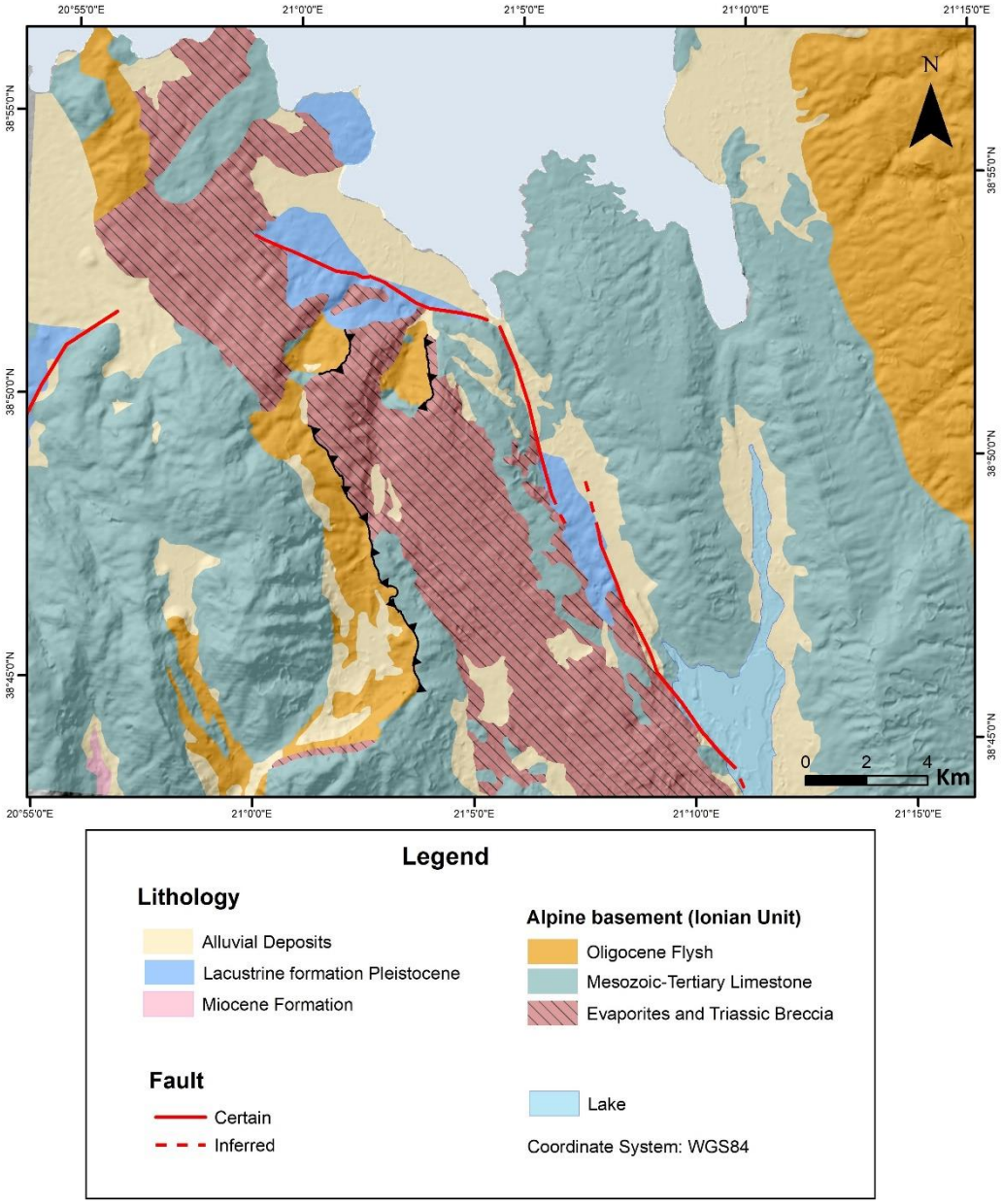

Figure 4 Neotectonic map of Amfilochia area modified after Katsavrias (1984a,b) and Papnikolaoy and Lekkas 1997.

places, gypsum breccias are in close spatial association with carbonates conglomerates. Stratigraphically overlying is the upper Triassic “Pantocrator facies” limestones which are locally dolomitic, and they are either massive or brecciated. In the Toarcian, the reddish to yellowish Ammonitico Rosso limestones was deposited. In the mid Jurassic (Dogger) the Ionian has become a deep marine area where the thin-bedded limestones with chert intrercalations, the so called “Vigla formation” is deposited. From the mid Cretaceous to late Eocene the sedimentation includes mostly thin bedded limestones with chert intercalations or clastic limestones with fragments of fossils from shallower marine areas. The flysch deposition began in the latest Eocene and continued through the Oligocene and in places up to the early Miocene (Aquiatanian).

In the Plio-Pleistocene post-alpine sediments have deposited on the alpine rocks of the Ionian Unit. These include clayey-pelites, thin bedded to non-bedded light-yellow to green marls, along the margin of in Katouna valley light colored marls occur locally grading into breccio-conglomerates. The Quaternary deposits such as terra rossa from limestone erosion, scree, old and new talus cones and weathering materials from adjacent rocks, alluvial deposits, unconsolidated fluvial deposits sandy-clayey materials, sands and pebbles in the torrent and river beds recent coastal deposits and marshy areas reflect a strong deposition environment variety with silt and humid soils.

The central part of Katouna valley is filled with alluvial deposits whereas along the margins screes and talus cones can be observed. Below these recent sediments older Plio-Pleistocene rocks are exposed, thus placing a time constraint for the age of Katouna valley. At the northern edge of the valley, along the southern margin of Amvrakikos gulf, alluvial deposits and recent alluvial fan and screes appear. In few places, Plio-Pleistocene conglomerates and lacustrine marls were also observed.

It is necessary to examine the Quaternary and Plio-Pleistocene sediments because the scientific field of Neotectonics or the Earthquake Geology examines the movements of Quaternary and especially the recent tectonic movements. The neotectonic movements can be identified by (Papapetrou- Zamani, 1995): The deformation of the geological layers from other sediments of Quaternary or Pre-Quaternary period, such as the Triassic breccias. The deformation of surface elements and especially marine, lacustrine and fluvial terraces with recent age, evidence of lacustrine deposits which correlate with the elongated lakes along the strike of fault. The neotectonic movements can cause changes to the hydrological network like circumvention of the river-bed, reversal river-flow, lake creation, formation of terraces into the river valleys, changes to the underground water by alternation to their flow line (Papapetrou-Zamani, 1995). This study has had (Gkardi, 2011), (Vassilakis et al.,2011) and (Perouse, 2016).

Earth Observation System, SAR Interferometry and GPS

Earth observation Systems and the display of earth surface have two main categories. The difference between the two is the source of radiation that they record. The first called passive system which detect the electromagnetic radiation which is the result of the reflection of solar radiation. These systems could record the physical radiation. This type of energy is known as the thermal infa-red segment of the electromagnetic spectrum. It can be recorded day and night but the problem is the amount of energy which is needed to become "visible" from the sensors. The red part of the electromagnetic spectrum is the part which had very low wavelengths. The second called active systems and they are based on the reflection of electromagnetic waves, emitted by another external source e.g. by the radar receiver itself. These systems cover the invisible part of the electromagnetic spectrum. Microwave frequencies are available in that part of spectrum. Usually the Recording system is what emits the energy to the earth's surface and reflected, returns and records the echo of the signal. These systems like Radar emitting in the microwave frequency. One of the advantages of active systems are that they have the ability to used day and night, in all weather conditions (Parcharidis, 2015).

Furthermore, the science which dealing with the observation of earth's surface from space is the Remote Sensing. Remote sensing is the science or maybe better the art, of acquiring information about earth's surface without touching it. This is done by sensing and recording, reflected or emitted energy and processing, analyzing and applying that information. In addition, for the process is available an interaction between the emitted radiation and the targets of interest. (Avery & Berlin, 1992).

The first requirement for remote sensing is to have an energy source to illuminate the target, this energy is in the form of electromagnetic radiation. Two characteristics of electromagnetic radiation are particularly important for

understanding remote sensing. These are the wavelength and frequency. Electromagnetic radiation consists of an electrical field(E) which varies in magnitude in a direction perpendicular to the direction in which the radiation is traveling, and a magnetic field (M) oriented at right angles to the electrical field. Both these fields

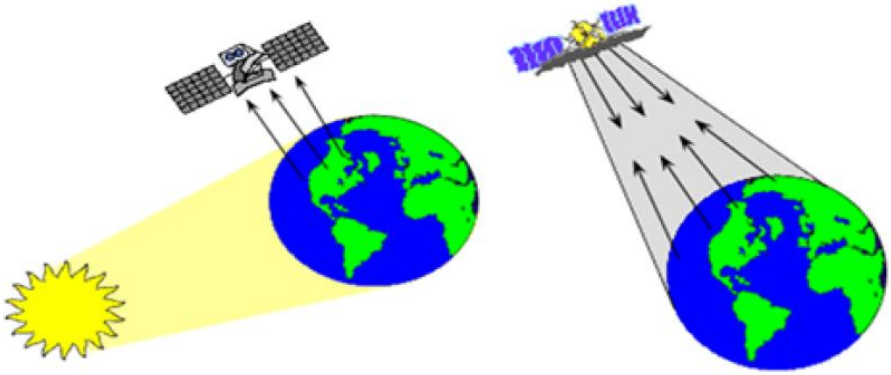

Figure 5 Active and passive systems from Natural Resources Canada, 2016

travel at the speed of light (c) (Natural Resources Canada, 2016).

SAR Sensors

There are two types of sensors in remote sensing systems. As before, the sun is a source of radiation. The sun is very useful for remote sensing, because it provides us a very convenient source of energy. The two types of sensor are the passive and the active. As passive sensors called the sensors which measure energy which is naturally available. These sensors could record the reflected energy only during the day when the sun is up to the sky. As active sensors, called the sensor which could provide their own energy source for illumination. These sensors could be obtaining measurements anytime and recording microwave lengths. Synthetic aperture radar(SAR) sensors are represent the best example for an active sensor. They are emitted in the microwave part of the electromagnetic spectrum. Microwaves have wavelengths in the millimeter to meter range (Parcharidis, 2016).

The basic principle is that an antenna, mounted on a platform, transmits a radar signal in a side-looking direction towards the Earth's surface. The echo, which is the reflected signal, is backscattered from the ground and received later at the same antenna (monostatic radar). The receiver is also the transmitter and is usually the same antenna. For SAR sensors, the amplitude and the phase of the received signal are recorded. These two elements are necessary to the next step, the processing of the signal. The radar signal is emitted by pulses. Pulses are transmitted from radar platform as it moves along the azimuth direction. The extent of the pulse is limited in time, illuminating a narrow strip of the surface. The reflected signal is some of the energy which is scattered back to the radar instrument. The different of the size of antenna change the antenna beam. The smaller antenna, the bigger the beam can be. Also, the beam is characterized by the frequencies of waves (Natural Resources Canada, 2016).

In addition, to achieving resolution in range, it is useful to ent a narrow pulse to resolve close targets. By transmitted the signal, a "chirped" signal could be produced, if pulse can't be narrow. The transmitted pulses are usually coded

waveforms with significant bandwidth. Matched filtering allows the recovery of fine resolution features with a low peak-power pulse train.

Radar (Radio Detection and Ranging) remote sensing uses the microwave portion of the electromagnetic spectrum, from a frequency of 0.3 GHz to 300 GHz, or in wavelength terms, from 1 m to 1 mm. Most remote sensing radars operate at wavelengths between .5 cm to 75 cm. The microwave frequencies have been arbitrarily assigned to bands identified by letter. The most popular of these bands for use by imaging radars include:

- X-band: from 2.4 to 3.75 cm (12.5 to 8 GHz). Widely used for military reconnaissance and commercially for terrain surveys. Used on CV-580 SAR (Environment Canada).
- C-band: from 3.75 to 7.5 cm (8 to 4 GHz). Used in many spaceborne SARs, such as ERS-1 and RADARSAT.
- S-band: from 7.5 to 15 cm (4 to 2 GHz). Used in Almaz.
- L-band: from 15 to 30 cm (2 to 1 GHz). Used on SEASAT and JERS-1.
- P-band: from 30 to 100 cm (1 to 0.3 GHz). Used on NASA/JPL AIRSAR.

The choice of Radar frequency depends on the application which you would like to study. For small features, like ice discrimination, could use X-band, for large features, like the geology mapping, could use L-band, for very small features, like foliage penetration, could use low frequencies so P-band. The C-band is a good compromise.

Considering the frequencies, there are some advantages and some disadvantages. For example, low frequencies correspond more difficult in the stage of processing, they need larger antennas and feeds. On the other hand, high frequencies need more power and the have more difficult electronics. Also, they need good component availability at X-band (Natural Resources Canada, 2016).

Also, it is necessary to refer the polarization. Its origin is the orientation of the electric vector of an electromagnetic wave. SAR system antennas can transmit and receive either horizontally or vertically polarized electromagnetic radiation. The SAR sensors have the polarization of both waves in the same direction, is referred to as like-polarized. It should be noted that, when the wavelength interacts with the ground surface and is scattered from it, the polarization can be modified. The properties of ground are the reason of the modification. Basic SARs have only one polarization VV (for vertical transmitted and vertical received) or HH (for horizontal transmitted and horizontal received) (Natural Resources Canada, 2016).

Synthetic Aperture Radar (SAR)

Synthetic Aperture Radar (SAR) is a microwave imaging system. Due to uses microwaves, it has capabilities to bypasses the weather conditions and the cloud cover. This behavior leads to minimum or zero decline of the microwave radiation during its pass from the atmosphere (Drury, 1987). Night and operational capabilities because it is an active system. Finally, its 'interferometric configuration', Interferometric SAR or InSAR, allows accurate measurements of the radiation travel path because it is coherent. Measurements of travel path variations as a function of the satellite position and time of acquisition allow generation of Digital Elevation Models (DEM) and measurement of centimetric surface deformations of the terrain (Ferretti et al., 2007).

SAR takes advantage of the Doppler history of the radar echoes generated by the forward motion of the spacecraft to synthesize a large antenna. This allows high azimuth resolution in the resulting image despite a physically small antenna. As the radar moves, a pulse is transmitted at each position. The return echoes pass through

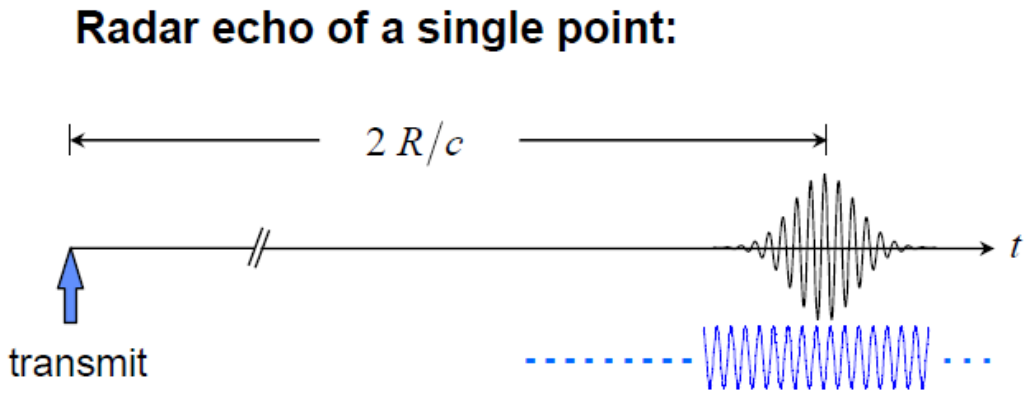

Figure 6 Radar echo

the receiver and are recorded in an echo store.

The frequency stays stable as the radiation emitted through materials with different density. The velocity and the wavelength don't have the same attitude with the frequency (Parcharidis, 2016).

Furthermore, in order to give the acquisition geometry of SAR systems, it is known that the satellite sensors are mounted on their platforms with the direction of transmission orthogonal to that flight direction. A satellite carries a radar with the antenna pointed to the Earth's surface in the plane perpendicular to the orbit. The inclination of the antenna with respect to the nadir is called the off-nadir angle and in contemporary systems is usually in the range between 20° and 50°. The off-nadir angle is never zero, since the radar would receive the echoes from the imaged objects at nearly the same time, make it impossible to create an image. Due to the curvature of the Earth's surface, the incidence angle of the radiation on a flat horizontal terrain is larger than the off-nadir angle. The direction along the Line of Sight (LOS) is usually called the slant-range direction. The antenna footprint moves at the satellite speed along its orbit (Ferretti et al., 2007).

SAR images represent an estimate of the radar backscatter for that area on the ground. Darker areas in the image represent low backscatter, while brighter areas represent high backscatter. Bright features mean that a large fraction of the radar energy was reflected back to the radar, while dark features imply that very little energy was reflected.

In SAR image, each pixel has both amplitude and phase values; the amplitude value records the radar brightness "speckle effect" in range direction, the backscattered energy of the pulse informs about the radar contribution of that pixel (Bouraoui, 2013).

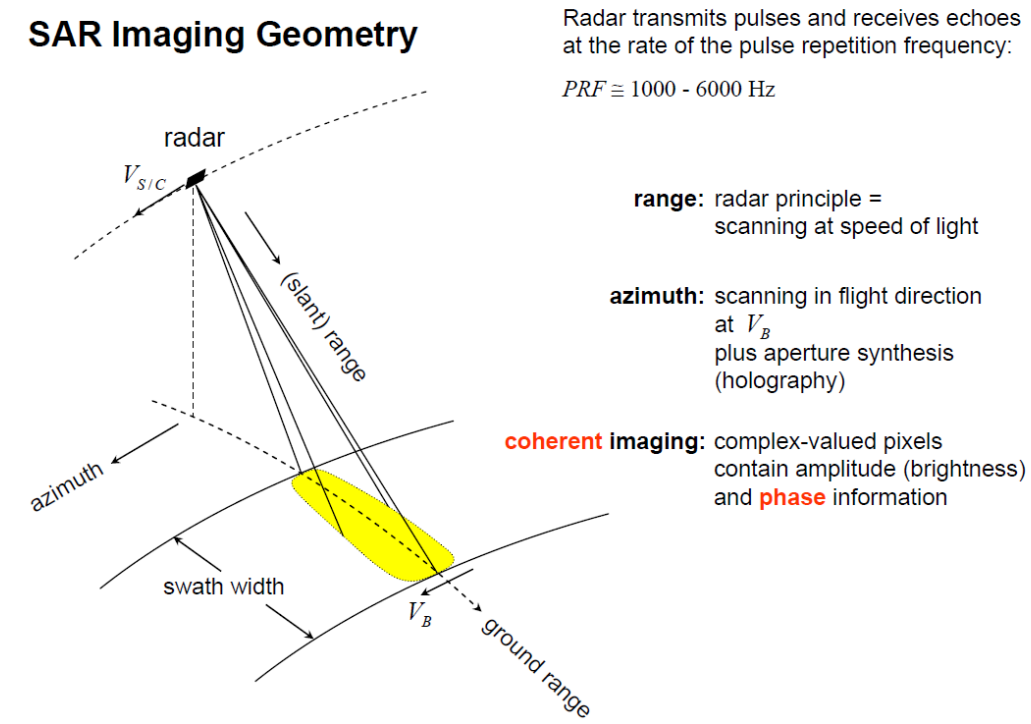

Figure 7 SAR Imaging Geometry from DLR

ERS Satellite

The European Remote Sensing satellite ERS-1, launched in July 1991, carried a comprehensive payload including an imaging synthetic aperture radar. ERS-2, which overlapped with ERS-1, was launched in 1995. Both ERS satellites were built with a core payload of two specialized radars and an infrared imaging sensor. The two were designed as identical twins with one important difference: ERS-2 included an extra instrument to monitor ozone levels in the atmosphere.

Shortly after the launch of ERS-2 in 1995 ESA decided to link the two satellites in the first 'tandem' mission which lasted for nine months. During this time, the increased frequency and level of data available to scientists offered a unique opportunity to observe changes over a very short space of time, as both satellites orbited Earth only 24 hours apart.

The near-polar orbit of ERS in combination with the Earth's rotation (E-W) enables two acquisitions of the same area to be made from two different look angles on each satellite cycle. If just one acquisition geometry is used, the accuracy of the final DEM in geographic coordinates strongly depends on the local terrain slope, and this may not be acceptable for the final user. Combining DEMs obtained from ascending (S-N) and descending (N-S) orbits can mitigate the problems due to the acquisition geometry and the uneven sampling of the area of interest, especially on areas of hilly terrain (this is illustrated in Figure 1-14 on page A-15). The ERS antenna looks to the right, so for example a slope that is mainly oriented to the West would be foreshortened on an ascending orbit, hence a descending orbit should be used instead.

In March 2000, a computer and gyro control failure led to ERS-1 finally ending its operations, after far exceeding its planned lifetime. In July 2011, ERS-2 was retired and the process of deorbiting the satellite began(http://www.esa.int/Our_Activities/Observing_the_Earth/ERS_overview).

Figure 8 An artistic expression of ERS-2 (http://www.esa.int/ESA)

Envisat Satellite

The Envisat Satellite launched on 1 March 2002. Envisat's largest single instrument was the Advanced Synthetic Aperture Radar (ASAR), operating at C-band. This ensures continuity of data after ERS-2, despite a small (31 MHz) central frequency shift. It features enhanced capability in terms of coverage, range of incidence angles, polarization, and modes of operation. The improvements allow radar beam elevation steerage and the selection of different swaths, 100 or 400 km wide. Envisat was in a 98.54° sun-synchronous circular orbit at 800 km altitude, with a 35-day repeat and the same ground track as ERS-2.

, Envisat had 10 instruments to provide continuous observation and monitoring of Earth's land. The most important instrument was the ASAR (Advanced Synthetic Aperture Radar). It was the largest single instrument on board. Operating in the C-band, it ensured continuity of data after ERS-2.

The other nine instruments were

- MERIS (Medium Resolution Imaging Spectrometer): an imaging spectrometer that measured the solar radiation reflected by Earth at a ground spatial resolution of 300 m, with 15 spectral bands in visible and near infra-red and programmable in width and position. MERIS allowed global coverage of Earth every three days. The primary mission of MERIS was the measurement of sea colour in oceans and coastal areas.
- AATSR (Advanced Along Track Scanning Radiometer): an infrared radiometer providing high resolution and high accuracy temperature information, for applications such as sea surface temperature or fire observation.
- SCIAMACHY: an imaging spectrometer whose primary mission objective was to perform global measurements of trace gases in the troposphere and stratosphere.

- MIPAS (Michelson Interferometer for Passive Atmospheric Sounding): an instrument that looked further into the infrared part of the spectrum and complemented SCIAMACHY. It provided information on additional trace gases and atmospheric temperatures.
- GOMOS (Global Ozone Monitoring by Occultation of Stars): dedicated to atmospheric monitoring, GOMOS was a medium resolution spectrometer that primarily measured stratospheric ozone.
- DORIS (Doppler Orbitography and Radio-positioning Integrated by Satellite): a microwave tracking system that was used to determine the precise location of the Envisat satellite.
- RA-2 (Radar Altimeter): an instrument for determining the two-way delay of the radar echo from Earth's surface to a very high precision - less than a nanosecond. It also measured the power and shape of the reflected radar pulses MWR: a microwave radiometer that measured integrated atmospheric water vapour column and cloud liquid water content, as correction terms for the radar altimeter signal. In addition, MWR measurement data are useful for the determination of surface emissivity and soil moisture over land, for surface energy budget investigations to support atmospheric studies, and for ice characterisation.
- LRR (Laser Retro Reflector): a passive device which was used as a reflector by ground-based SLR stations using high-power pulsed lasers. In the case of Envisat, tracking using the LRR was mainly accomplished by the International Laser Ranging Service (ILRS).

At April 2012, the communication with the Envisat satellite was suddenly lost. Despite continuous commands sent from a widespread network of ground stations, there had been no reaction from the satellite(http://www.esa.int/Our_Activities/Observing_the_Earth/Envisat/Mission_overview).

Figure 9 An artistic impression of ENVISAT (http://www.esa.int/ESA)

Synthetic Aperture Radar (SAR) Interferometry

A satellite SAR could behold the same area from different look angles. This result can be achieved either with two radars systems in the same platform or at different times by exploiting repeated orbits of the same satellite (Fletcher, 2007). The tool to detect and monitor ground displacement or to retrieve information about the local topography is by using SAR images and phase measurements. With these, the Digital Elevation Model (DEM) for the area can be estimated. The estimation of the DEM and the monitoring of surface deformation phenomena are the two-different applications stem from the hypothesis: measuring phase variations by comparing two SAR images acquired over the same area (Ferretti, 2014).

Another significant issue in InSAR analyses is the importance of knowledge of the sources of noise in InSAR. Atmospheric effects and phase decorrelation, and the fact that any interferometric measurement is meaningful only if phase values can be unwrapped, are the sources of noise in SAR Interferometry (Ferretti, 2014).

SAR Interferometry can be used to estimate topography of an area of interest or to detect surface deformation patterns. The sensitivity, however, is quite different. Local topography can be estimated with an accuracy of a few meters, while displacement fields can be detected with an accuracy of a few millimeters.

Basic Principles

First, a SAR image is a matrix of complex numbers and phase values are related to the sensor-to-target distance. The distance between the two orbits of a satellite in the plane perpendicular to the orbit is called the interferometric baseline and its projection to the slant range is the perpendicular baseline.

The basic idea behind InSAR is the phase value φ of a pixel P of a radar image. The function of the phase has four different contributions:

$$\Phi(P) = \varphi + (4\pi/\lambda)\, r + \alpha + v$$

where:

- φ is the phase contribution due to the nature and the location of all elementary scatterers within the resolution cell associated to pixel P coherently adding to form the radar return.
- $4\pi r/\lambda$ is the most important contribution for any interferometric analysis. Whenever there is a dominant scatterer within the resolution cell, r is the sensor-to-target distance, λ is the wavelength.
- α is a phase contribution which does not introduced yet. The travel time of the radar pulse is affected by the medium the e.m. wave propagates through. Free particles in the ionosphere and clouds, water vapour, rain, fog in the troposphere, affect the speed of propagation of the signal and introduce as a result effects on the phase detected by the receiving antenna (Goldstein, 1995, Tarayre and Massonet, 1996, Hanssen, 2001). With this factor may compromise the quality of the final results.

- ***v*** is a phase contribution related to any noise source. Noise sources are mentioned before. The thermal noise is the most important type of noise.

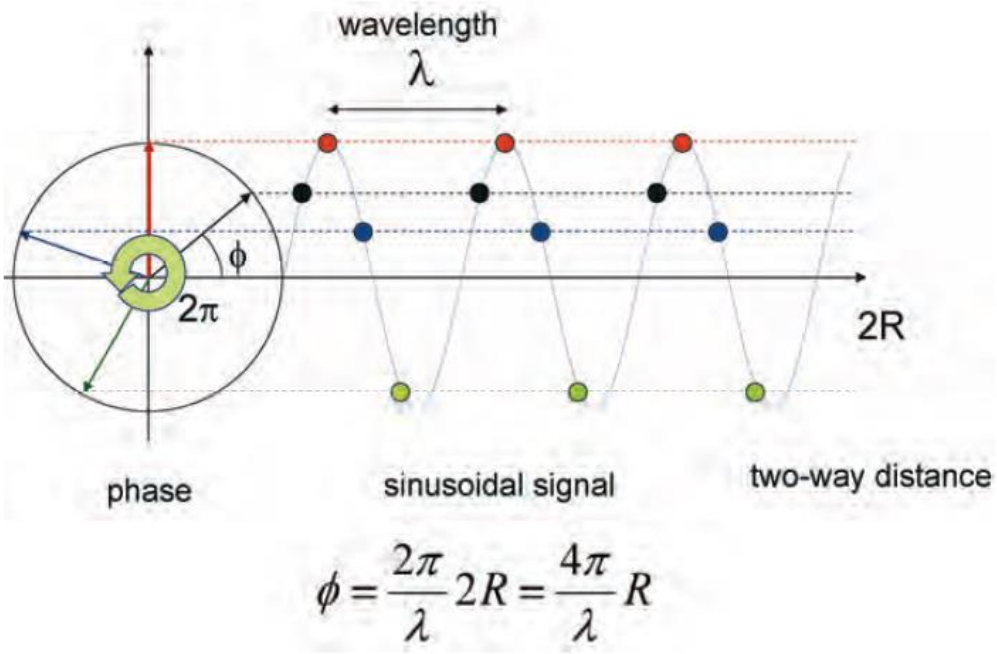

Figure 10 A sinusoidal function sin φ is periodic with a 2π radian period. (http://www.esa.int/ESA)

The thermal noise depends on the signal-to-noise ratioand is related to the level of the thermal noise of the radar system and the power of received signal. This factor is stronger when the radar echo is weaker.

With SAR Interferometry, the phase values of two separate SAR images are compared and some useful information from that correlation can be extracted. So, the answer to this effort is to compute the difference of phase values pixel P of two SAR images, supposing they have been properly co-registered, so that homologous pixels correspond to the same resolution cell (Ferretti, 2014).

Calculating the phase difference of two SAR images on a pixel-by-pixel basis, it is become the generation of an interferogram. According to Ferretti et al., 2007, the phase difference is expressed by:

$$\Delta\Phi(P) = \Delta\varphi + (4\pi/\lambda)\,\Delta r + \Delta\alpha + \Delta v$$

After the hypothesis that nothing has changed between the two acquisitions: all the scatterers have not moved or changed their dielectric constant and no significant variations of atmospheric conditions have affected the second radar acquisition. The above function simply become:

$$\Delta\Phi\,(P) = (4\pi/\lambda)\,\Delta r$$

This equation is shown that the unit of length of our measurements is the wavelength rather than the range resolution of the radar. Wherever you have a tool for measuring range variations, there are two applications:

- Looking the same area at different times, using the same acquisition geometry, to notice any possible ground displacement phenomena.
- Looking at the same object from two different points to estimate the third dimension.

On the other hand, the interferometric phase is a mixture of different signals: range variations, atmospheric effects, noise and possible variations of the reflectivity phase (ϕ). Whenever the phase of the reflectivity is the same in an image pair, the interferometric phase becomes powerful tool in measuring range variations due either different acquisition geometries or to target displacement (Ferretti et al., 2014). So, the InSAR measurements are also sensitive to topography, spatial separation between satellites and the electrical properties of the ground (Ferretti et al., 2001, Colesanti et al., 2003):

$$\Delta\varphi = \varphi_{flat} + \varphi_{topo} + \varphi_{orbit} + \varphi_{defo} + \varphi_{tropo} + \varphi_{iono} + \varphi_{scat} + \varphi_{noise}$$

where:

Δ_{φ} is interferometric phase (or phase change between SAR acquisitions)

φ_{flat} is flat earth phase

φ_{topo} is topographic phase contribution

φ_{orbit} is the phase error induced by errors in orbit information

φ_{defo} is phase contribution related to ground deformation

φ_{tropo} is tropospheric phase contribution

φ_{iono} is ionospheric phase contribution

φ_{scat} is phase contribution related to the scatterer's electrical properties

φ_{noise} is the combined noise term

Consequently, InSAR phase measurements are wrapped between –π and π, which is known as modulo 2π (Ferretti et.al, 2007). The proper number of phase cycles has to be estimated by means of a phase unwrapping algorithm. The process of adding the correct integer multiple of 2π to the interferometric fringes is called phase unwrapping. The aim of phase unwrapping is to recover the interger number of cycles k to be added to the wrapped phase ψ so that the phase value φ can be finally obtained for each image pixel:

$$\varphi = \psi + 2\pi * k$$

The continuous phase is the unwrapped phase. This phase can be only resolved by using additional information such as GPS measurements (Osmanoglu et al., 2016).

Another important factor for the SAR Interferometry is the signal-to-noise ratio (SNR). The level of noise in an interferogram depends on the SNR. SNR is expressed in terms of 'similarity' between the master and the slave image. The more similar the reflectivity values are, the higher SNR of the interferogram. Also, one

more factor is called coherence *γ*. The interferometric coherence is the measurement unit of the quality of results, namely the noise of phase and the ability of fringes appearance in an interferogram.

$$\gamma = \frac{E\{\alpha * \beta\}}{\sqrt{E\{\alpha_2\}E\{\beta_2\}}}$$

where E is the expectation operator. The coherence is related to SNR, and the equation is given:

$$\gamma = \frac{1}{1+SNR^{-1}}$$

The width of the coherence values ranges between 0 and 1. Very low values of coherence near to 0 correspond to a non- coherent image and very high values of coherence near to 1 correspond to a stable backscattered signal (Touzi et al., 1999). The noises areas are connected with low values of coherence. So, the value of the interferometric coherence is correlated with the noise which exists in an interferogram. Four decorrelation terms are linked to the total coherence:

$$\gamma_{total} = \gamma_{spatial} + \gamma_{Doppler} + \gamma_{temporal} + \gamma_{thermal}$$

where:

γ_{total} is total correlation, $\gamma_{spatial}$ is spatial baseline decorrelation, $\gamma_{temporal}$ is temporal decorrelation, $\gamma_{Doppler}$ is Doppler centroid decorrelation and $\gamma_{thermal}$ is thermal decorrelation.

The spatial baseline decorrelation is related to the horizontal separation between two satellite orbits. The temporal decorrelation is related to the regions where the volume dominant is permanent like forests. The Doppler centroid decorrelation is related to the satellite attitude and especially is affected when is

existed a difference between the master and the slave image (Osmanoglu et al., 2016).

Coherence maps can estimate the local SNR, but cannot highlight the presence of atmospheric effects. Estimation windows used for generating coherence maps are much smaller than the correlation length of disturbances, therefore, an interferogram can exhibit very high coherence values over most of the images pixels, while being heavily corrupted by atmospheric noise.

Differential SAR interferometry (DInSAR)

Until now, SAR interferograms could be used for DEM reconstruction and for the detection of surface deformation phenomena. For monitoring surface deformation, the demands are higher, firstly baseline-related phase contributions cannot usually be neglected and secondly, phase noise and atmospheric effects affect the estimation of actual displacement. But, when a digital elevation model is available, the impact of local topography on the interferometric phase can be limited by generating a differential interferogram.

The baseline-related phase components should be estimated and extracted. The interpretation of a differential interferogram is not easy because the non-perfect compensation of topographic term could produce possible DEM and baseline errors which could create spurious phase components. It is very important the geometrical baseline between the two satellites due to it is correlated with the accuracy of the DEM to be used to create a good interferogram (Ferretti, 2014).

In conclusion, a differential interferogram is an interferogram where baseline-related components have been estimated and removed using an a priori DEM. The reliability of any phase unwrapping procedure and, in general, the precision of the measurements obtained by creating a differential interferogram can be assessed either by using prior information and in situ observations or by using more than one data pair acquired over the same area of interest (Ferretti, 2014).

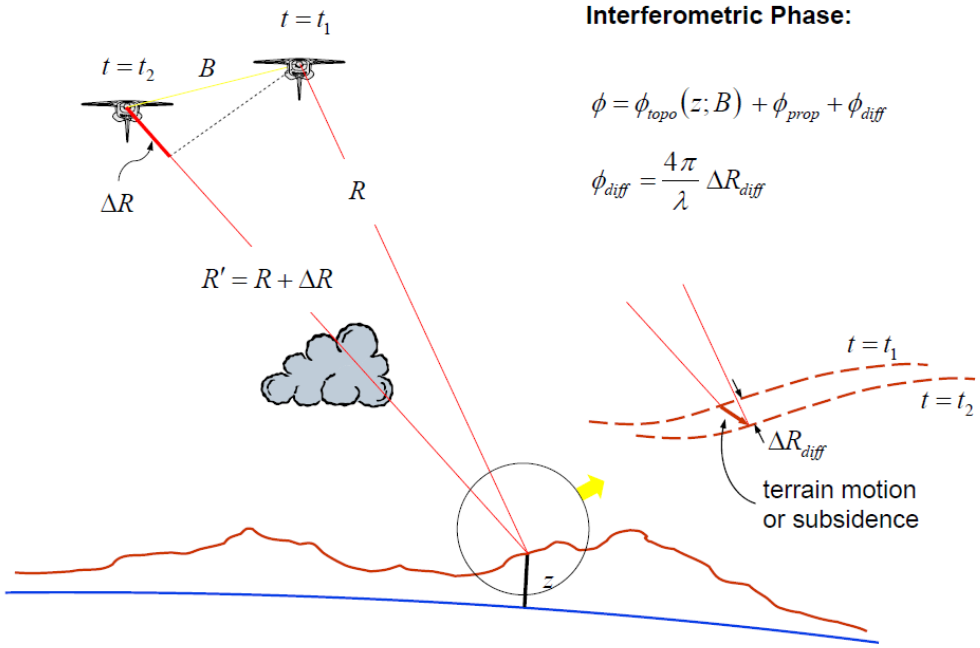

Figure 11 Geometry in DinSAR (DLR)

GPS Operation System

The Global Positioning System (GPS) is a U.S.-owned utility that provides users with positioning, navigation, and timing (PNT) services. This system consists of three segments: the space segment, the control segment, and the user segment. The U.S. Air Force develops, maintains, and operates the space and control segments.

The GPS space segment consists of a constellation of satellites transmitting radio signals to users. The United States is committed to maintaining the availability of at least 24 operational GPS satellites, 95% of the time. GPS satellites fly in medium Earth orbit (MEO) at an altitude of approximately 20,200 km (12,550 miles). Each satellite circles the Earth twice a day. The satellites in the GPS constellation are arranged into six equally-spaced orbital planes surrounding the Earth. Each plane contains four "slots" occupied by baseline satellites. This 24-slot arrangement ensures users can view at least four satellites from virtually any point on the planet.

The GPS control segment consists of a global network of ground facilities that track the GPS satellites, monitor their transmissions, perform analyses, and send commands and data to the constellation. The current operational control segment includes a master control station, an alternate master control station, 11 command and control antennas, and 16 monitoring sites.

The master control station in Colorado is where 2SOPS performs the primary control segment functions, providing command and control of the GPS constellation. The MCS generates and uploads navigation messages and ensures the health and accuracy of the satellite constellation. It receives navigation information from the monitor stations, utilizes this information to compute the precise locations of the GPS satellites in space, and then uploads this data to the satellites.

Monitor stations track the GPS satellites as they pass overhead and channel their observations back to the master control station. Monitor stations collect

atmospheric data, range/carrier measurements, and navigation signals. The sites utilize sophisticated GPS receivers and are operated by the MCS. There are 16 monitoring stations located throughout the world, including six from the Air Force and 10 from the National Geospatial-Intelligence Agency (NGA).

Ground antennas are used to communicate with the GPS satellites for command and control purposes. These antennas support S-band communications links that send/transmit navigation data uploads and processor program loads, and collect telemetry. The ground antennas are also responsible for normal command transmissions to the satellites. S-band ranging allows 2SOPS to provide anomaly resolution and early orbit support. There are four dedicated GPS ground antenna sites (http://www.gps.gov/systems/gps/).

GLONASS

GLONASS, or "Global Navigation Satellite System", is a space-based satellite navigation system operating in the radio navigation-satellite service. It provides an alternative to GPS and is the second navigational system in operation with global coverage and of comparable precision.

GLONASS is a global satellite navigation system, providing real time position and velocity determination for civilian users. The satellites are in middle circular orbit at 19,100 kilometers (11,900 mi) altitude with a 64.8-degree inclination and a period of 11 hours and 15 minutes. GLONASS' orbit makes it especially suited for usage in high latitudes (north or south), where getting a GPS signal can be problematic. The constellation operates in three orbital planes, with eight evenly spaced satellites on each. A fully operational constellation with global coverage consists of 24 satellites, while 18 satellites are necessary for covering the territory of Russia. To get a position fix the receiver must be in the range of at least four satellites (https://www.glonass-iac.ru/en/).

GPS Studies and Strain Analysis

The GPS data could provide information about the kinematics of deformation. The use of GPS velocities free from transient elastic strain can lead to estimates of the steady long-term crustal strain for a particular region (Chousianitis et al., 2015). The latter includes the seismic as well as potential aseismic processes and consequently, its integration into seismic hazard assessment provides a maximum estimate. However, aseismic processes should be treated with caution in such estimates because in the case of significant amount, the bias which they introduce in the long-term strain will ultimately lead to an overprediction of the actual seismic hazard.

The geological and seismological data show that in central Greece, active tectonics are dominated by widespread, NE-SW to N-S extension since Pliocene, forming a series of subparallel 100km long rifts such as the Gulf of Corinth. This extension is mostly accommodated by seismic slip along the large normal fault segments (20-30km in length), where the expected magnitudes are a function of the seismic potential of the hosting fault planes (Chousianitis et al., 2015).

The analysis of differenced GPS phase observations in 24h sessions to estimate loosely constrained station coordinates together with orbital and Earth orientation parameters and their associated covariance matrices, then the usage of daily loosely constrained bias- fixed solutions of the parameters and their associated covariance matrices as quasi-observations in GLOBK and after that, it was the introduction of the cleaned daily solutions for each GPS site into GLOBK in order to combine the individual epoch-by epoch solutions into one ‘’stacked’’ solution and obtain a consistent set of positions and velocities accounting for seasonal signals and offsets (Chousianitis et al.,2015).

Also, strain describes the geometric changes that take place during deformation and therefore its knowledge in terms of pattern and amplitude is

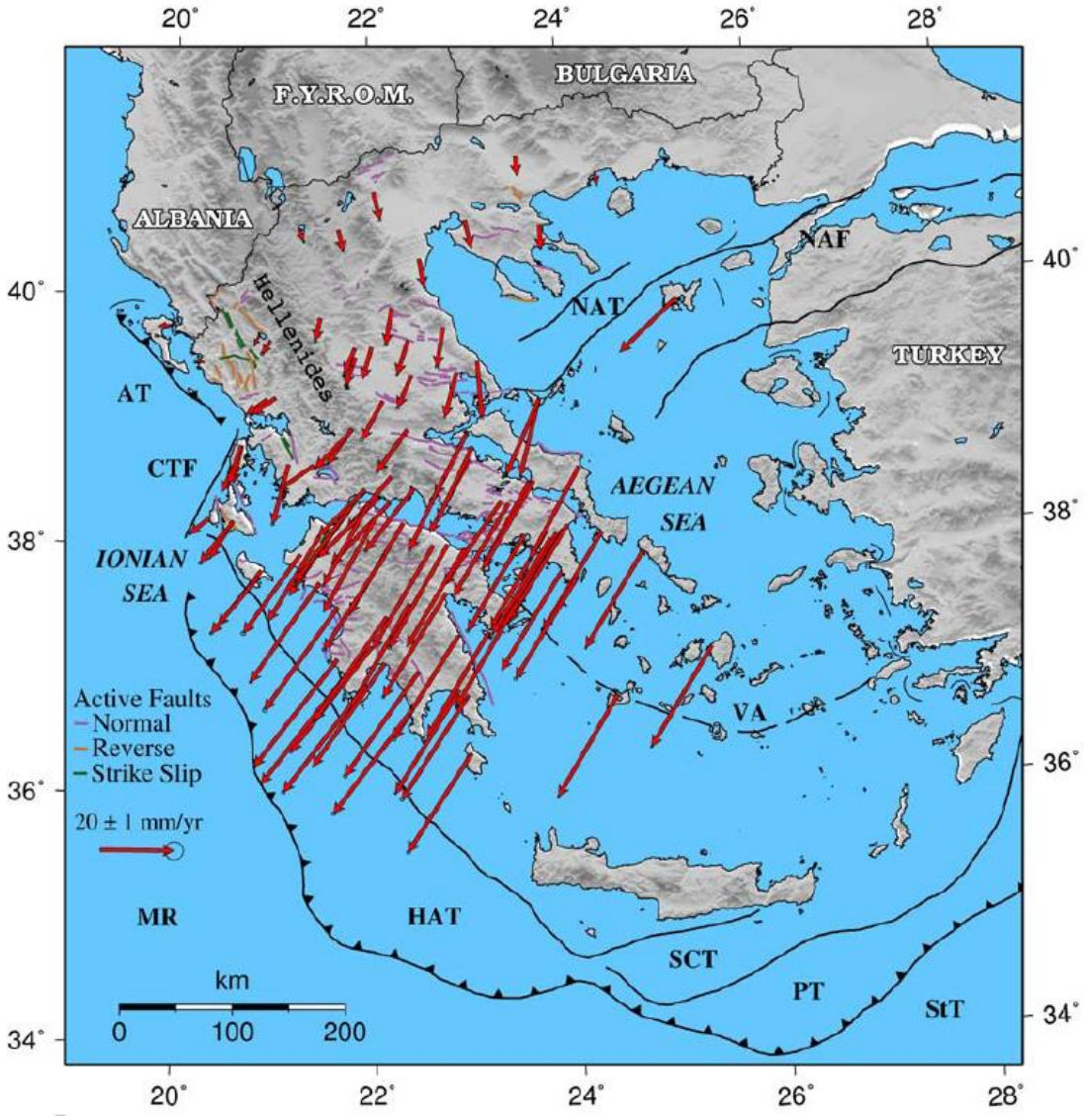

Figure 12 Horizontal GPS velocity vectors relative to stable Eurasia from Chousianitis et al., 2015. Error ellipses represent 95 per cent confidence level. Abbreviations are as follows: NAT, North Aegean Trough; NAF, North Anatolian Fault; AT, Apulian Thrust; CTF, Cephalonia Transform Fault; MR, Mediterranean Ridge; HA, Hellenic Arc System; SCT, South Cretan Trough; PT, Pliny Trench; StT, Strabo Trench.

important for understanding the ongoing tectonic activities in an area (Chousianitis et al., 2015).

In the above figure, there are the principal axes (eigenvectors and eigenvalues) of the horizontal two-dimensional strain rate tensor. More specifically, the eigenvectors are depicted with their directions in red color is an eigenvalue is positive, which means extension and in blue color the negative values, which means compression.

The largest extension can be observed in the western and central part of the Corinth rift (around 200-250 ns/yr), while extension rates decrease rapidly toward east (Attica) and north (Thessaly) (Clarke et al., 1998, Avallone et al., 2004). In terms of extension direction, it is observed a 90^{o} switch from the N-S and E-W direction in the region south of the Gulf of Corinth.

Especially, for the broader area of the study, it can be concluded that this area does not rotate as a single rigid body; instead, two internal rotations (domains A and B) dominate the present-day pattern. Since both domains rotate clockwise, the 50 % larger rotation of domain A with respect to domain B provides a differential rotation that induces left-lateral shear in the Akarnania region and contributes to the formation of the sharp boundary of shear strain at this region (Chousianitis et al., 2015). The Akarnania shear belt strikes NW-SE and is characterized by sinistral motion. In this area, it should be noted that a NW-SE straight line was drown for simplification, although the development of second-order structures such as the “pull-apart” basin of Trichonis Lake, has taken place.

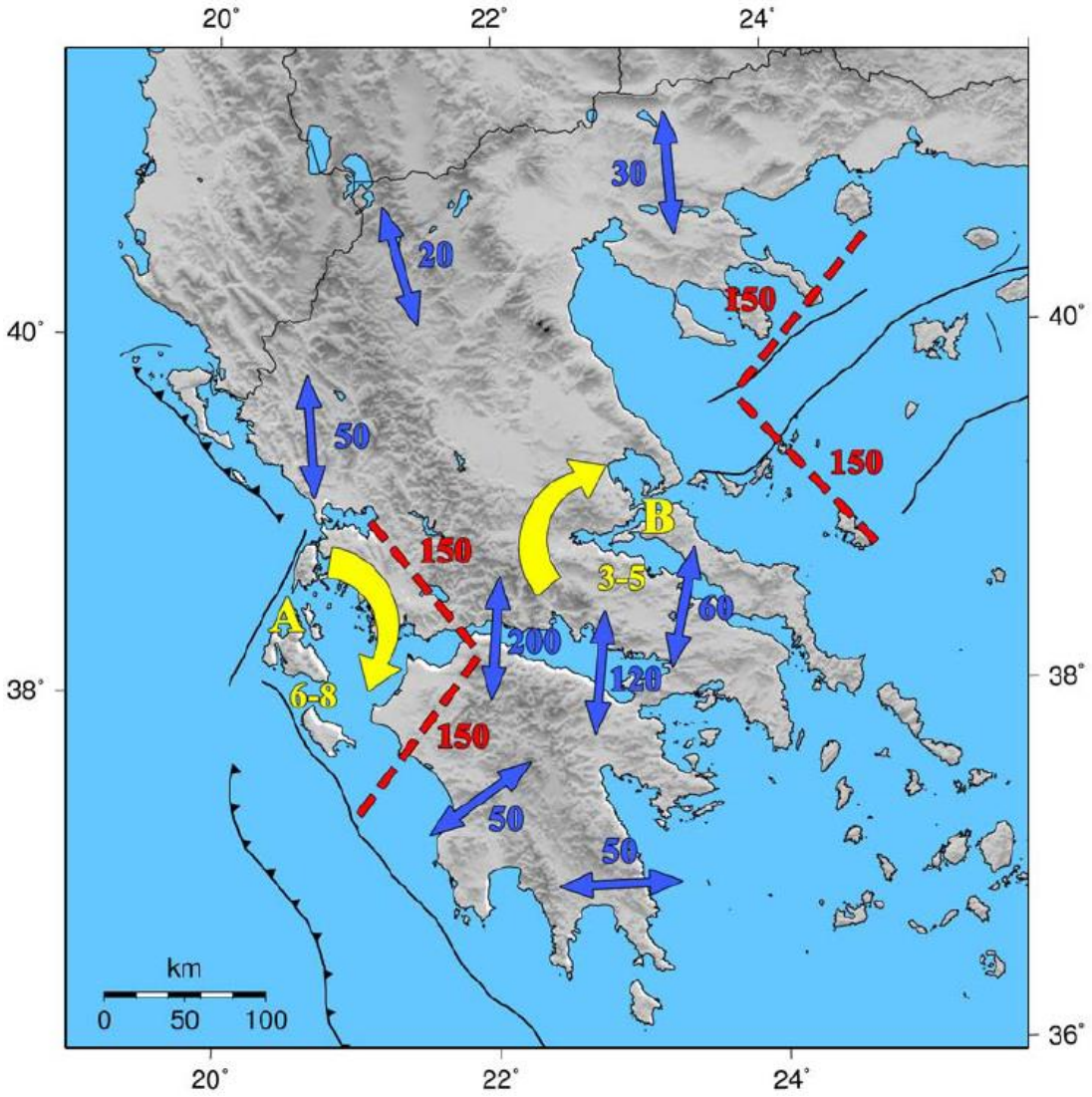

Figure 13 Model of the kinematics of the present-day crustal deformation in Central and Western Greece proposed from Chousianitis et al., 2015. Yellow colors correspond to rotation rates (numbers are degrees/Myr), blue colors to extension rates (numbers are ns/yr) and red colors to maximum shear strain rates (numbers are ns/yr).

Geological Data

The geological data which are presented in this chapter refer to field observations and field measurements. The first aim of this study is to precisely locate the Katouna Fault Zone (KFZ) in the field and to identify fault scarps and the fault surface associated with this fault. Another important goal of this thesis was to define the kinematics of the KFZ with field observations and measurements. In order to achieve this, the mapping of the broader area of Aitoloakarnania was necessary. So, the fault trace was mapped and studied along the Amvrakikos Gulf - Amvrakia Lake transect. Additionally, all the fault planes that were detected in the vicinity were also analysed.

Along the observed fault scarp the main lithology is the evaporites and specifically, the Triassic evaporites and the evaporite breccia of the Ionian Unit. In the broader area, the geological formations mainly consist of Mesozoic limestones, evaporites and quaternary deposits to the east of KFZ. Also, the western fault block of the KFZ mainly consists of limestone and evaporite breccia. In some places, the limestone is intensely brecciated. This breccia hosts shear fractures especially near the fault scarps. On these fractures, slickensides can be observed being parallel and sub-parallel to the dip direction of the fractures, eg, these fractures represent oblique- to dip-slip faults. Extensional or open fractures are also common within this tectonic breccia. These fissures have an opening of a few centimeters and strike E-W to NE-SW. The dip is almost vertical, and the dip direction of these joints is 82^{o}/322^{o} with slickensides plunging towards 315^{o}. All the above-mentioned data, were taken west of probable KFZ trace on the Akarnanika mountains and in an area near the fault zone. This breccia stretches a few meters to the west and it ends to the Triassic evaporites along the Katouna valley.

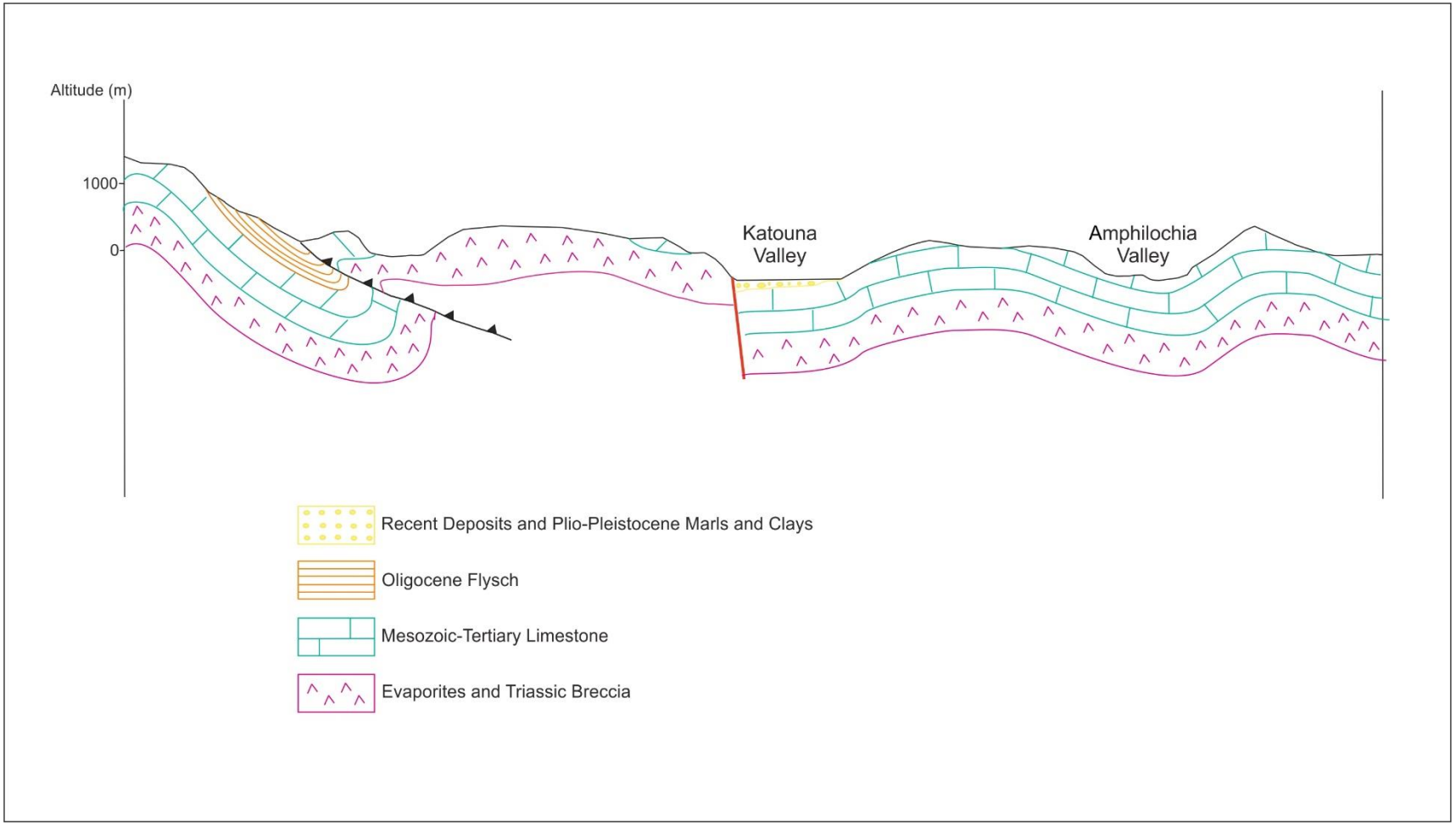
Altitude (m)
1000
0
Katouna Valley
Amphilochia Valley
Recent Deposits and Plio-Pleistocene Marls and Clays
Oligocene Flysch
Mesozoic-Tertiary Limestone
Evaporites and Triassic Breccia

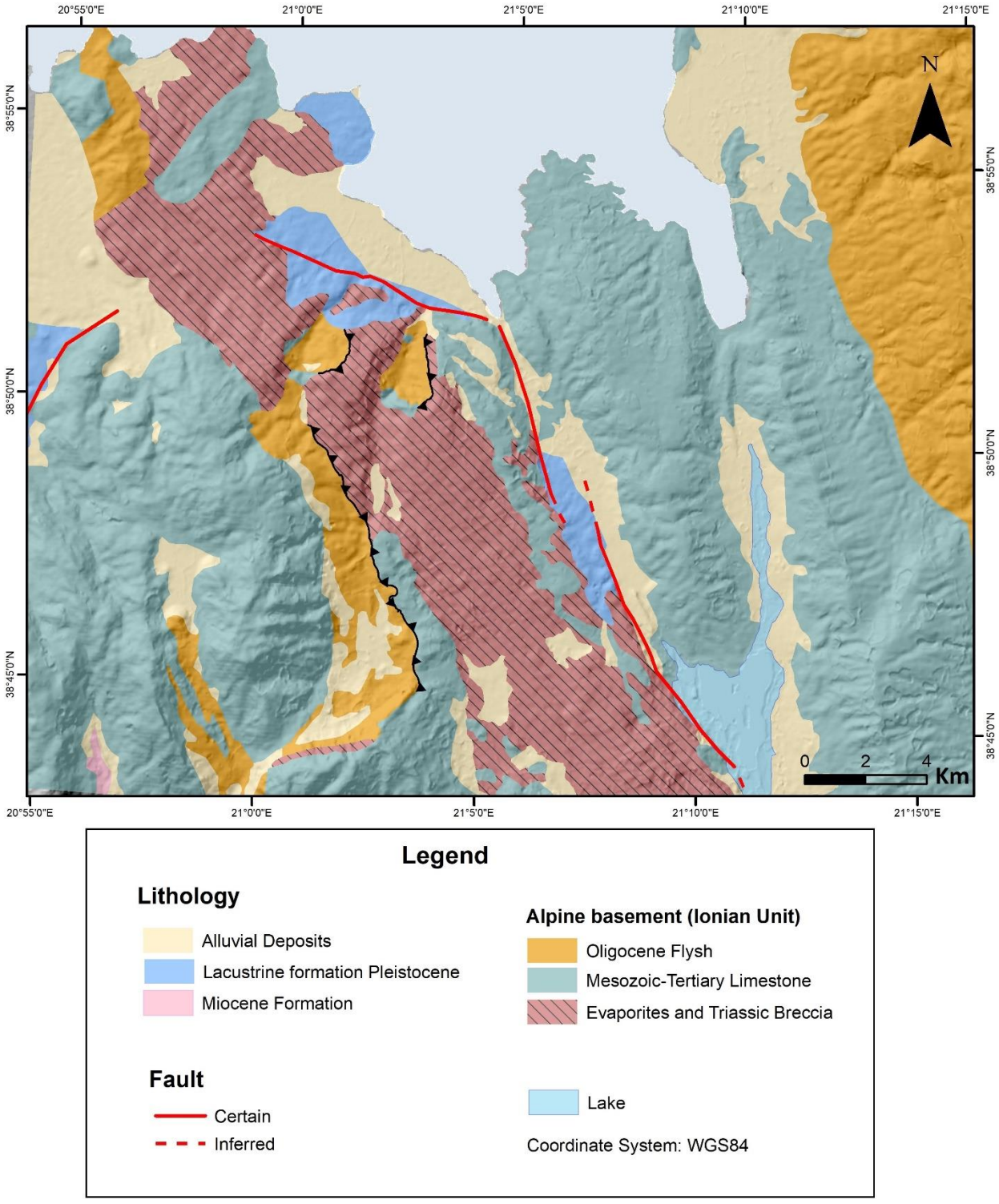

Figure 14 Revised neotectonic map of Katouna area modified after Lekkas et al., 1997

Katouna Fault Zone

The Katouna Fault Zone does not appear to have a continuous fault scarp, and this is probably related to the fact that it is formed in the evaporite. Evaporites deform in a ductile manner even in the upper crust, so most probably this is the main reason why the Katouna Fault Zone, has not formed a continuous fault surface. Instead, several discrete surfaces were identified along the fault zone from Lake Amvrakia to Amvrakikos Gulf. All the fault surfaces on evaporite layer were measured. On these discrete surfaces, two kinds of slickensides were observed: a weak dip-slip lineation and a dominant almost strike-slip lineation.

Based on field measurements, the KFZ strikes NNW-SSE and it is generally

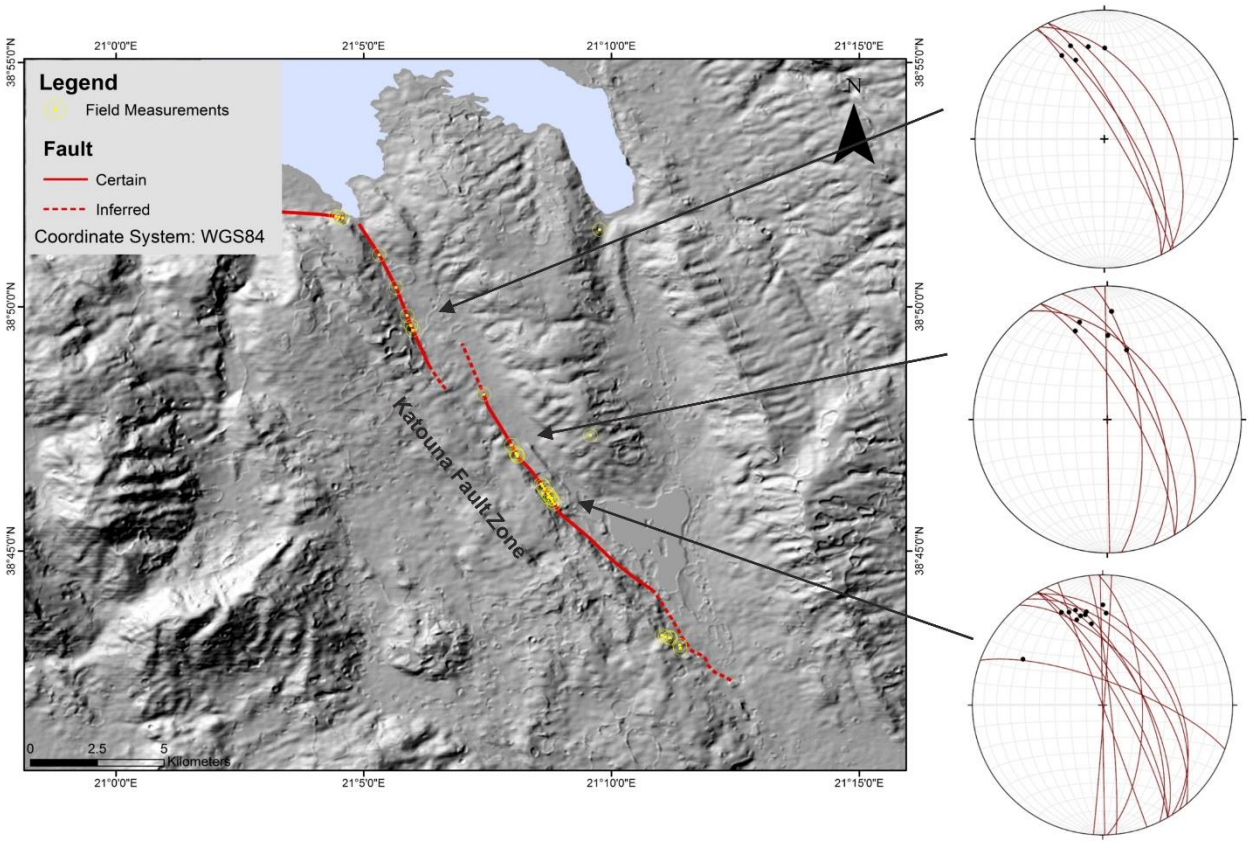

Figure 15 Stereoplot (lower hemisphere projection) of the Katouna Fault Zone fault planes and associated slickensides.

Table 1 Measurements of the fault plane and the slickensides

dipping steeply (~80^{o} degrees) towards the ENE. The strike-slip slickenlines on the fault planes are plunging towards the NNW. Numerous kinematic indicators such as grooves, ridge-in-groove lineations, tectonic clasts preserved on the fault surface reveal that the Katouna Fault zone is a left-lateral strike-slip fault. The best exposure of the fault surface is near the Amvrakia Lake and east of the Katouna village. Further west, no clear exposure of the fault appears within the Mesozoic limestone.

	Katouna Fault Zone		Secondary Subordinate Faults	
	Fault Plane	Slickenside	Fault Plane	Slickenside
1	90/089	25/358	50/060	35/040
2	85/058	32/343	50/054	37/052
3	89/094	30/002	60/070	45/032
4	90/070	45/333	60/318	60/280
5	80/060	30/335		
6	65/060	25/344		
7	75/060	30/349		
8	60/050	23/325		
9	80/054	22/330		
10	83/059	28/350		
11	76/064	24/340		
12	85/084	12/346		
13	75/020	30/300		
14	65/088	30/000		
15	65/064	28/344		
16	75/058	35/342		
17	75/054	22/336		
18	70/084	20/009		
19	83/075	30/345		
20	85/091	29/352		

Also, the field measurements of the fault surfaces are included in Table 1. Except of these main fault planes which belong and form the KFZ, several secondary subordinate fault surfaces were identified and measured. The slickensides on fault surface reveal that the vertical movement is dominant, and these faults are characterized as normal faults. Their kinematics are compatible with the general kinematics of the KFZ.

From the geomorphological point of view, there is evidence which helps identifying the fault scarp. The scarp crosses the main part of Katouna valley and juxtaposes the alpine basement against the quaternary deposits. In this study, a fault is considered as “active” if it controls the landscape morphology at first order (offset streams, structural landscape, upward convex-shaped profile, etc.) and/or if it offsets Quaternary deposits. By opposition, a fault is considered as “inactive” when the landscape morphology results mainly from erosional processes. Consequently, it is very possible that the KFZ represents an active fault zone. The KFZ is a segment of Katouna-Stamna Fault zone (KSFZ), which crosscuts the central region of Aitoloakarnania from Gulf of Amvrakikos near Loutraki at the north, to Aitoliko area at the south. The fault shows no clear “earthquake-related” scarps (Perouse et al., 2016).

In the following field photos the discrete fault surfaces of the Katouna Fault zone can be seen.

Figure 16 Fault planes of KFZ with slickensides and tectonic clasts

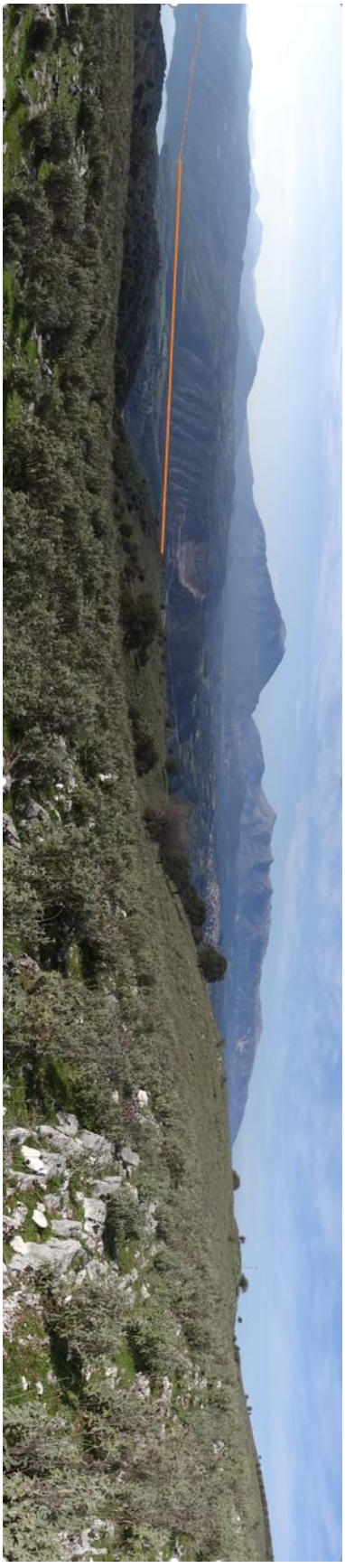

Figure 17 Panoramic view of the Katouna Fault in the field

Figure 18. The fault scarp of the Katouna Fault

Loutraki Fault

The northward termination of KFZ is onto the Loutraki fault. The Loutraki fault is ESE-striking fault and shows a typical morphology of an active normal fault with an associated fault scarp. The overall morphology can be simply interpreted as the result of footwall uplift and southward tilt associated with the northward dipping

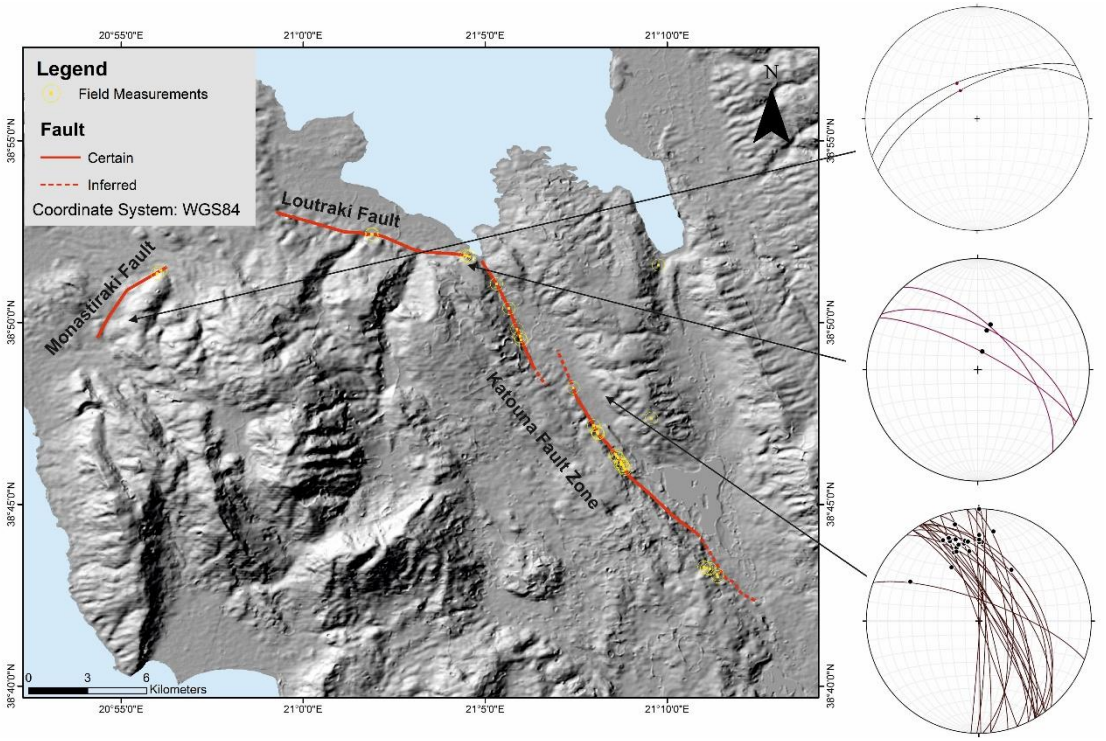

Figure 19 The display of Loutraki fault on map and the display of fault plane and slickenside in stereographic projection.

Loutraki normal fault.

Loutraki fault does not have a continuous fault surface for the same reason with the KFZ eg it is mostly hosted within the evaporites. Further along the strike of this fault limestones appear and there the fault plane is identified in some areas. It is a north-dipping fault with a main dip direction towards 035° and main dip of 65° degrees. Near the KFZ termination dip-slip slickensides were observed on the slip surface of Loutraki fault. The Loutraki fault juxtaposes the alpine bedrock against the quaternary deposits. Based on the above, the Loutraki fault is considered to be a north-dipping normal fault. Since it is situated along the southern coast of Amvrakikos Gulf it is very possible that it represents a boundary fault of the Amvrakikos graben.

	Loutraki Fault	
	Fault Plane	Slickenside
1	77/028	73/012
2	31/048	31/012
3	60/020	

Table 2 Measurements of the fault plane and the slickensides

According to Perouse et al., 2016 the Loutraki fault shows two benches that represent either several parallel migrating faults (i.e., “paleo” scarps) or interaction between footwall uplift and notching due to headward erosion from high stand sea levels. In either case, the location of the present-day active normal fault would be at the base of the escarpment. The actual fault can be observed only in two places.

Figure 20 Loutraki fault surface in limestone and associated slickensides

Monastiraki Fault

Monastiraki fault is a brittle structure away from the Katouna Fault Zone. It is a normal fault with a very well-developed slip surface. The strike of the fault is ENE-WSW. The main dip of the fault is 63º degrees and the main dip direction is 335º. On the slip surface slickensides which are parallel to sub-parallel to the dip direction can be observed. This fault is most probably correlated to the extensional structures which formed the graben of Gulf of Amvrakikos.

	Monastiraki Fault	
	Fault Plane	Slickenside
1	60/340	60/330
2	66/332	62/329

Table 3 Measurements of the fault plane and the slickensides

Figure 21 Monastiraki Fault surface in Mesozoic limestones

GPS Data

In this chapter, the GPS data published in the literature were used by Chousianitis et al., 2015, Hollenstein et al., 2008 and of the Master Thesis of Vlachou 2006. The map below interprets the kinematics of the regional faults with the help of geodesy. A possible correlation of these data with the InSAR results will be discussed later. In order to create this map, the calculation of the velocities in horizontal component was performed. To achieve this result, the velocities of North (V_N) and East (V_E) component were used to the calculation of the velocity of horizontal component (V_{hor}). The equation is shown below:

$$|V_{hor}| = \sqrt{V_N^2 + V_E^2}$$

Also, the azimuth of the direction of the motion was calculated. The estimation of azimuth was taking place after a set of transformations, which included the equations below:

$$\tan\theta = \frac{V_E}{V_N}$$

and

$$\tan^{-1}\frac{V_E}{V_N}$$

According to Chousianitis et al., 2015, the monitoring period was from 2003 to 2013, for Hollestein et al., 2008 was from 1993 to 2003 and for Vlachou, 2006 was from 1996 to 2006. These time periods were able to be correlated with the monitoring period of the SAR results.

According to the map, it is observed that the direction of motion is SW. In order to evaluate the existence of Katouna- Aitoliko fault zone, it is suggested that the fault zone delimits the change of the values of the velocities. So, in the western

block, the Akarnania block, the velocities are higher and show a motion to SW. In the eastern block, the direction of the motion is the same but the values of the velocities are changed. This fact is more intensive to the north part of Aitoloakarnania, where near the Amfilochia, the velocity is ~7mm/yr, but in the Akarnania block, the value ranges 12 to 16mm/yr. It is noteworthy that the velocities in Akarnania block are doubled compared with the values in the Amfilochia valley.

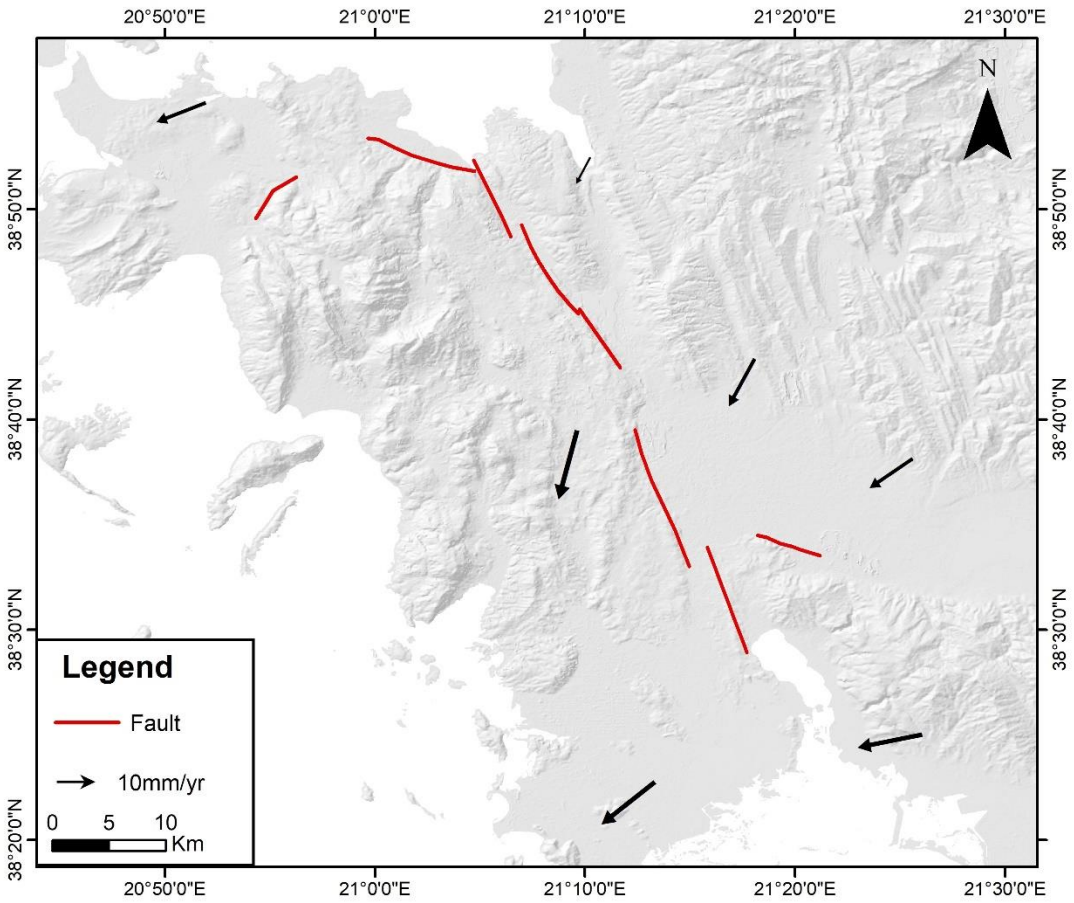

Figure 22 Horizontal GPS velocity vectors relative to stable Eurasia. The GPS data was taken from Chousianitis et al., 2015, Hollestein et al., 2008 and Vlachou 2006.

SAR Processing and Results

EOLi Platform - Datasets

At the beginning of this Master Thesis, I worked on the SAR processing. The first step was to collect all the available datasets of the study area. The satellites that the data selected from are the ENVISAT and ERS-2. For this aim, the download of the Eoli Platform, which is a java application, was necessary (https://earth.esa.int/web/guest/eoli).

The data products which are provided to us are (A) SAR data products, and especially, are ASA_IMS_1P and single look complex, downloaded directly from ESA's complete achieve due to the On-The-Fly (OFT) service. The selection for the datasets was taking place according to the track and the frame which are relative to the broader study area. So, from the EOLisa platform was collected all the available descending and ascending ENVISAT ASAR and ERS ASAR products for the area of interest. For ENVISAT ASAR was collected two different datasets for descending

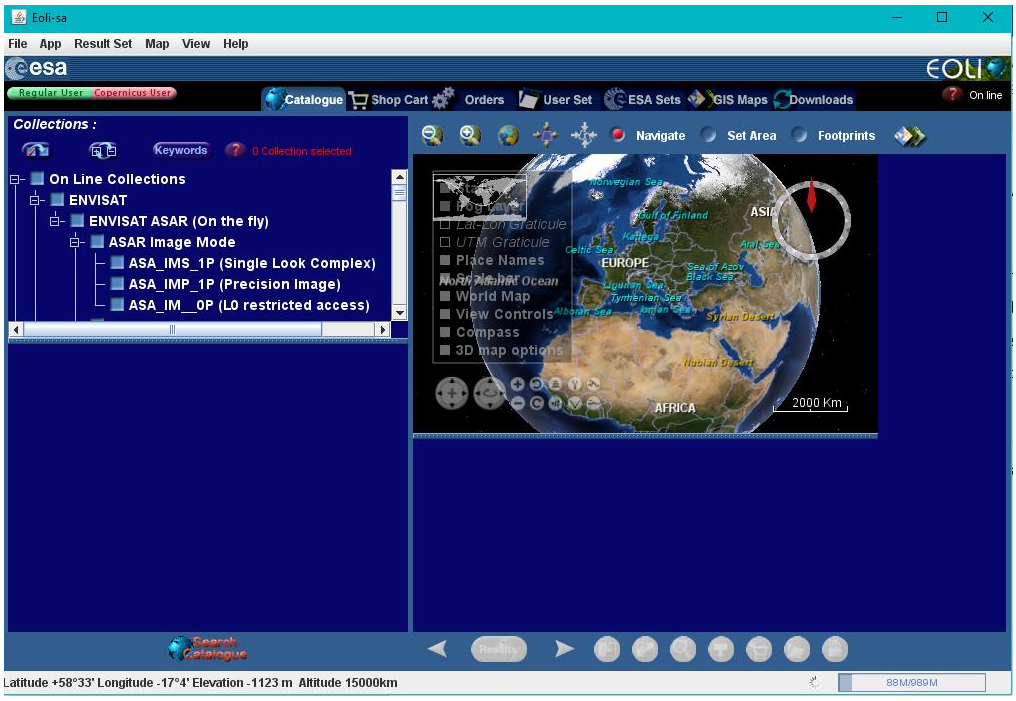

Figure 23 Environment of Eoli-sa platform

images in order to investigate the differential movement of Katouna fault zone.

Number of Images	Satellite	Date	Track	Frame	Polarization	Pass
1	ENVISAT	17/11/2002	180	765	VV	Ascending
2	ENVISAT	06/04/2003	180	765	VV	Ascending
3	ENVISAT	20/07/2003	180	765	VV	Ascending
4	ENVISAT	24/08/2003	180	765	VV	Ascending
5	ENVISAT	28/09/2003	180	765	VV	Ascending
6	ENVISAT	07/12/2003	180	765	VV	Ascending
7	ENVISAT	25/04/2004	180	765	VV	Ascending
8	ENVISAT	26/12/2004	180	765	VV	Ascending
9	ENVISAT	19/02/2006	180	765	VV	Ascending
10	ENVISAT	09/07/2006	180	765	VV	Ascending
11	ENVISAT	31/12/2006	180	765	VV	Ascending
12	ENVISAT	04/02/2007	180	765	VV	Ascending
13	ENVISAT	15/04/2007	180	765	VV	Ascending
14	ENVISAT	13/07/2008	180	765	VV	Ascending
15	ENVISAT	17/08/2008	180	765	VV	Ascending
16	ENVISAT	19/04/2009	180	765	VV	Ascending

Table 4 Dataset ENVISAT ASAR for ascending orbit

Number of Images	Satellite	Date	Track	Frame	Polarization	Pass
1	ENVISAT	25/08/2003	322	2817	VV	Descending
2	ENVISAT	21/01/2004	322	2817	VV	Descending
3	ENVISAT	31/03/2004	322	2817	VV	Descending
4	ENVISAT	09/06/2004	322	2817	VV	Descending
5	ENVISAT	14/07/2004	322	2817	VV	Descending
6	ENVISAT	18/08/2004	322	2817	VV	Descending
7	ENVISAT	27/10/2004	322	2817	VV	Descending
8	ENVISAT	05/01/2005	322	2817	VV	Descending
9	ENVISAT	16/11/2005	322	2817	VV	Descending
10	ENVISAT	01/03/2006	322	2817	VV	Descending
11	ENVISAT	27/09/2006	322	2817	VV	Descending
12	ENVISAT	01/11/2006	322	2817	VV	Descending
13	ENVISAT	08/08/2007	322	2817	VV	Descending
14	ENVISAT	05/11/2008	322	2817	VV	Descending
15	ENVISAT	03/06/2009	322	2817	VV	Descending

Table 5 Dataset ENVISAT ASAR for descending orbit

Number of Images	Satellite	Date	Track	Frame	Polarization	Pass
1	ENVISAT	02/05/2003	50	2835	VV	Descending
2	ENVISAT	19/09/2003	50	2835	VV	Descending
3	ENVISAT	24/10/2003	50	2835	VV	Descending
4	ENVISAT	02/01/2004	50	2835	VV	Descending
5	ENVISAT	30/07/2004	50	2835	VV	Descending
6	ENVISAT	08/10/2004	50	2835	VV	Descending
7	ENVISAT	17/12/2004	50	2835	VV	Descending
8	ENVISAT	28/10/2005	50	2835	VV	Descending
9	ENVISAT	02/12/2005	50	2835	VV	Descending
10	ENVISAT	10/02/2006	50	2835	VV	Descending
11	ENVISAT	17/03/2006	50	2835	VV	Descending
12	ENVISAT	26/05/2006	50	2835	VV	Descending
13	ENVISAT	30/06/2006	50	2835	VV	Descending
14	ENVISAT	13/10/2006	50	2835	VV	Descending
15	ENVISAT	22/12/2006	50	2835	VV	Descending
16	ENVISAT	26/01/2007	50	2835	VV	Descending
17	ENVISAT	03/04/2007	50	2835	VV	Descending
18	ENVISAT	21/03/2008	50	2835	VV	Descending
19	ENVISAT	21/11/2008	50	2835	VV	Descending
20	ENVISAT	26/12/2008	50	2835	VV	Descending
21	ENVISAT	06/03/2009	50	2835	VV	Descending
22	ENVISAT	06/11/2006	50	2835	VV	Descending
23	ENVISAT	19/02/2010	50	2835	VV	Descending
24	ENVISAT	04/06/2010	50	2835	VV	Descending

Table 6 Dataset ENVISAT ASAR for descending orbit

Number of Images	Satellite	Date	Track	Frame	Polarization	Pass
1	ERS-2	28/05/1995	186	765	VV	Ascending
2	ERS-2	06/08/1995	186	765	VV	Ascending
3	ERS-2	10/09/1995	186	765	VV	Ascending
4	ERS-2	15/10/1995	186	765	VV	Ascending
5	ERS-2	24/12/1995	186	765	VV	Ascending
6	ERS-2	25/01/1996	186	765	VV	Ascending
7	ERS-2	12/05/1996	186	765	VV	Ascending
8	ERS-2	16/06/1996	186	765	VV	Ascending
9	ERS-2	21/07/1996	186	765	VV	Ascending
10	ERS-2	29/09/1996	186	765	VV	Ascending
11	ERS-2	10/08/1997	186	765	VV	Ascending
12	ERS-2	19/10/1997	186	765	VV	Ascending
13	ERS-2	17/05/1998	186	765	VV	Ascending
14	ERS-2	26/07/1998	186	765	VV	Ascending
15	ERS-2	02/05/1999	186	765	VV	Ascending
16	ERS-2	11/07/1999	186	765	VV	Ascending
17	ERS-2	19/09/1999	186	765	VV	Ascending
18	ERS-2	28/11/1999	186	765	VV	Ascending

Table 7 Dataset ERS ASAR for ascending orbit

Number of Images	Satellite	Date	Track	Frame	Polarization	Pass
1	ERS-2	07/06/1995	322	2817	VV	Descending
2	ERS-2	12/07/1995	322	2817	VV	Descending
3	ERS-2	16/08/1995	322	2817	VV	Descending
4	ERS-2	20/09/1995	322	2817	VV	Descending
5	ERS-2	25/10/1995	322	2817	VV	Descending
6	ERS-2	29/11/1995	322	2817	VV	Descending
7	ERS-2	03/01/1996	322	2817	VV	Descending
8	ERS-2	07/02/1996	322	2817	VV	Descending
9	ERS-2	26/06/1996	322	2817	VV	Descending
10	ERS-2	22/01/1997	322	2817	VV	Descending
11	ERS-2	02/04/1997	322	2817	VV	Descending
12	ERS-2	07/05/1997	322	2817	VV	Descending
13	ERS-2	20/08/1997	322	2817	VV	Descending
14	ERS-2	24/09/1997	322	2817	VV	Descending
15	ERS-2	29/10/1997	322	2817	VV	Descending
16	ERS-2	07/01/1998	322	2817	VV	Descending
17	ERS-2	18/03/1998	322	2817	VV	Descending
18	ERS-2	07/04/1999	322	2817	VV	Descending
19	ERS-2	12/05/1999	322	2817	VV	Descending
20	ERS-2	16/06/1999	322	2817	VV	Descending
21	ERS-2	25/08/1999	322	2817	VV	Descending
22	ERS-2	29/09/1999	322	2817	VV	Descending
23	ERS-2	02/11/1999	322	2817	VV	Descending

Table 8 Dataset ERS ASAR for descending orbit

Software and Processing

GAMMA Remote Sensing Software

The software that took place the processing of the descending and ascending images was the GAMMA Remote Sensing Software. GAMMA Software supports the entire processing chain from SAR raw data to products such as digital elevation models, displacement maps and land use maps.

The GAMMA Software includes several Modules, each one consisting of documented, well-structured code. The software is understood as a toolbox that provides a wide functionality to support the user in the setting up of his processing tasks. Programs can be run individually on the command line or they can be called from scripts that permit running processing sequences in a more automated and efficient way.

The GAMMA software is grouped into four main modules: Modular SAR Processor (MSP), Interferometry, Differential Interferometry and Geocoding (ISP/DIFF&GEO), Land Application Tools (LAT) and Interferometric Point Target Analysis (IPTA). In addition, the SAR image co-registration and geocoding functionality is also available as a separate GEO package (https://www.gamma-rs.ch/).

SAR Processing

In this study, were applied two different interferometric techniques: the multi-interferometric Stacking (IS) (Strozzi et al., 2001) and the Interferometry through Single Value Decomposition (SVD) or Hybric Method (Berardino et al., 2002). Due to limited a-priori knowledge of the deformation regime of the area, a preliminary analysis by means of interferometric stacking technique (averaging of phases) was considered essential. Such analysis offers the opportunity to obtain a first estimation of the deformation pattern, and to recognize relatively stable areas which could be used as a reference in the subsequent point target analysis.

The software used to process the SAR images was the GAMMA Remote Sensing Software. This software allows processing of SAR, interferometric SAR (InSAR) and differential interferometric SAR (DInSAR) data for airborne and spaceborne SAR systems. During the processing, both interferometric techniques are followed step by step in order to produce an interferogram.

The first one, namely, the multi-interferometric Stacking technique (IS) is based on the calculation of the phase of a stack of individual interferograms through time to eliminate any possible uncorrelated temporal fluctuations of the interferometric phase. This procedure is well-known among the scientific community (Zebker et al., 1997, Fujiwara et al., 1998, Sandwell & Price, 1998) and suggests an alternative for the conventional differential interferometric SAR (DInSAR). IS ultimately produces a single displacement map through the combination of multiple differential interferograms. The main advantage of this method over conventional DInSAR is better performance in areas of low coherence and in anticipating for any atmospheric distortions.

The second technique, Singular Value Decomposition (SVD), is a hybrid method based on the mathematical concept of singular value decomposition (Banerjee S. and Roy A. 2014) to resolve timeseries of wrapped displacement phases.

As a method, it closely resembles a combination of conventional SAR interferometry technique, such as Small Baseline Interferometry (SBAS) and Permanent Scatterers Interferometry (PSI). SVD is a multi-reference stacking procedure which combines and analyzes wrapped interferograms, produced using conventional DInSAR, through the least squares method (application of SVD) to create a "single-reference" timeseries. Furthermore, the average displacement velocity is computed in the least squares regression step and is provided to the end-user (Usai, 2003).

Concerning the processing, the steps that applied were the generation of the differential interferograms, the filtering using an adaptive filter for the reduction of the phase noise, the unwrapping, the baseline refinement and finally the stacking for the method of Interferometric Stacking (IS). For the SVD method, the steps that applied were the same but in the end of processing applied the Singular Value Decomposition (SVD) method.

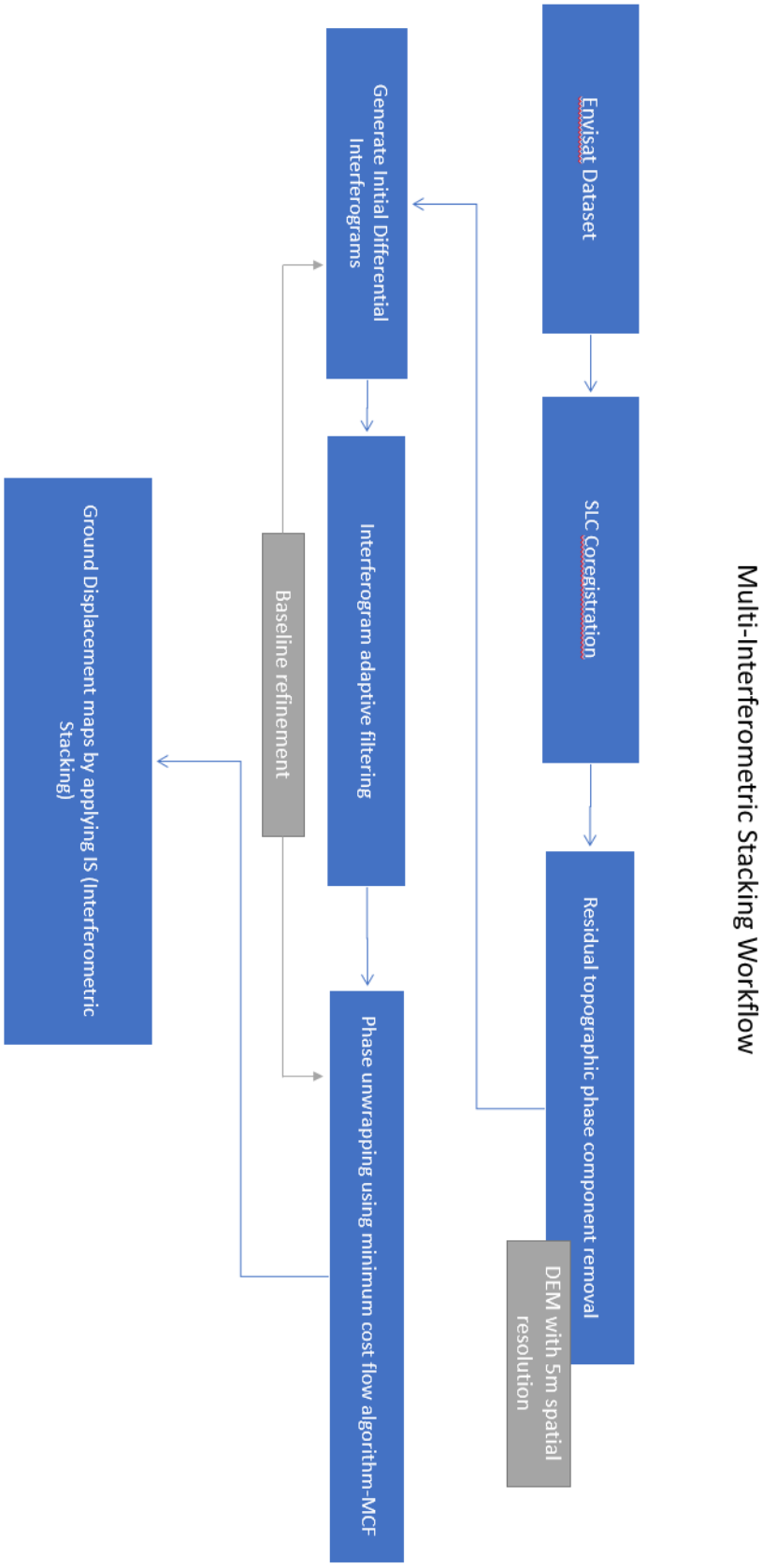

Figure 24 Multi-Interferometric Stacking Workflow

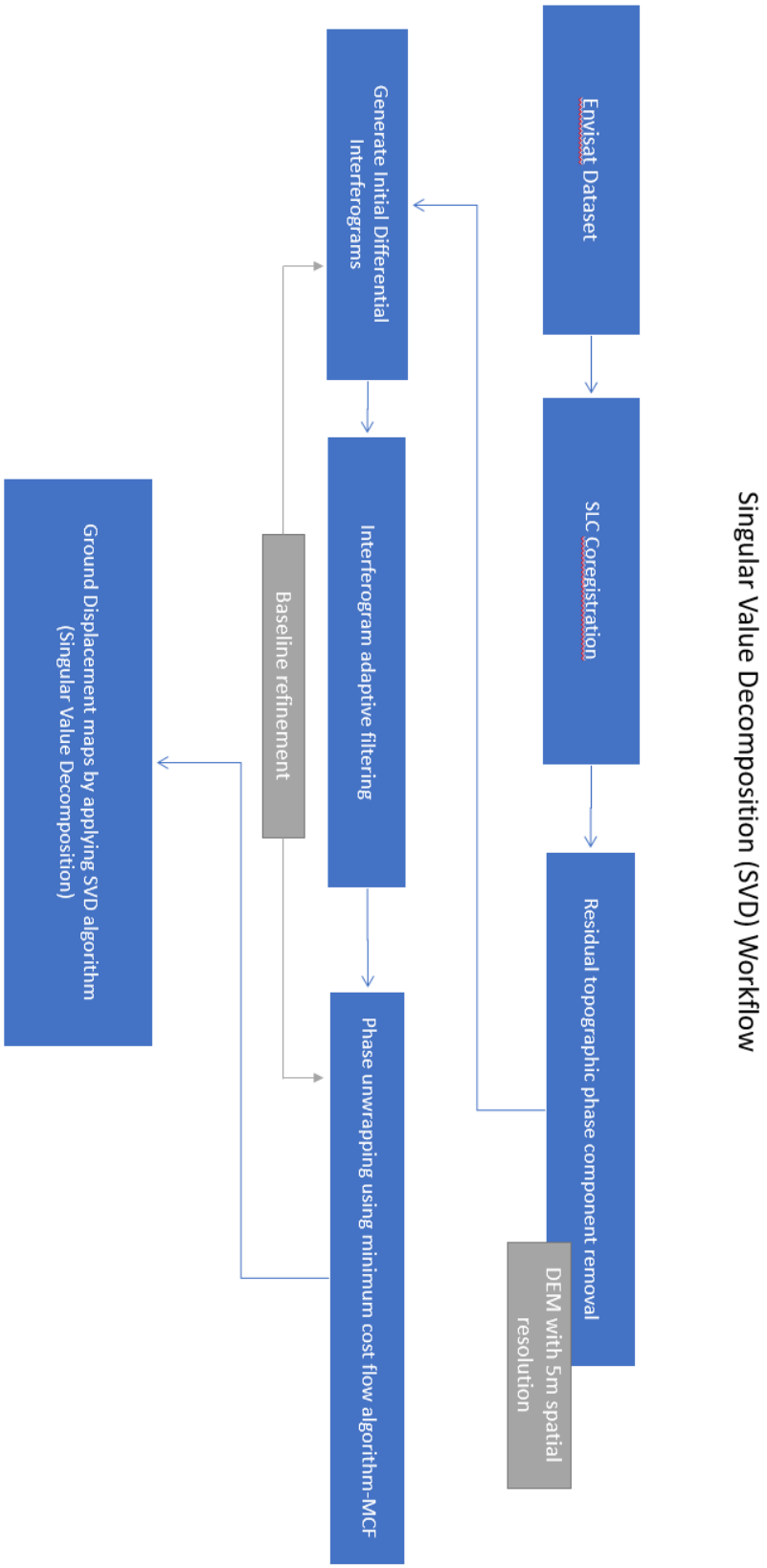

Figure 25 Singular Value Decomposition Workflow

Based on aforementioned flowcharts of the processing, the stages of the processing are analyze below (Wegmüller et al., 1998):

I. Data transcription and modification. SLC images indicate that each pixel corresponds to a single look and is a complex number. The format of an SLC depends on the SAR processor used. After transcription of the data from support media to the computer, modification of the SLC to adapt it to the interferometric processor used is necessary in most cases. Modification also includes taking a subset of an SLC.

II. Manipulation of orbital state vectors. State vectors are typically provided with the image data by the data processing facilities and include instant position and velocity of the satellite components expressed in the Earth-centered Cartesian coordinate system.

III. Co-registration. The SLCs forming an image pair do not overlap so that the computation of the interferogram requires first a co-registration step so that corresponding pixels in the two images perfectly match. Co-registration of the stack of images of every track by registering them to a chosen scene from the average image of the timeseries.

IV. Filtering of the frequency of SAR images for the maintenance of the common part of the electromagnetic spectrum so to the direction of range, as to the direction of azimuth. The aim of filtering in a processing is the improvement of the coherence of the interferometric phase. Flattening of the interferogram consists of removing the phase component due to the variation of the range distance across the image.

V. Production of the differential interferograms by multiplications of the complex part of the SAR images.

VI. Estimation of the removal of the flat Earth component from the interferograms based on the geometry of the interferometric pairs.

VII. Simulation of the topography and its removal from the differential interferograms by using the available digital elevation model and the

interferometric geometry of the topography. The first step of the simulation is the precision orbits and then the second step is the redefinition of the geometry by improving the estimation of the baselines.

VIII. Adaptive spatial filtering of the frequency of the differential interferograms by applying window resolution of 64 x 64 pixels.

IX. Estimation of the ambiguity of the phase by using the wrapped phase of the differential interferograms with level of ambiguity ≥ 0,3.

X. Improvement of the initial estimation of the baselines by the wrapped differential phases and re-estimation of the geometry of the interferometric pairs.

XI. Tranformation of the wrapped phase to vector and geocoding of the results to the selected map geographical projection by using the available digital elevation model.

XII. Evaluation and quality control of the interferograms, in order to remove these with high atmospheric distributions.

Interferometric processing for the selected study area was performed using ENVISAT and ERS-2 scenes. Initial estimates of the interferometric baselines were calculated from available precise orbit state vectors from Centre de Traitement Doris Poseidon (CTDP) (DORIS Precise Orbits) for ENVISAT and Delft Institute (NL) for Earth-Oriented SpaceResearch (DEOS) (Scharoo and Visser, 1998). The topographic phase was simulated based on SRTM v2 DEM of approximate spatial resolution of 90 m.

Consequently, all the datasets of ENVISAT ASAR and ERS ASAR had their properties. For the whole dataset of 16 ENVISAT ASAR ascending scenes, a perpendicular baseline of 250m is used to produce the interferometric stacking. The time period was from 2002 to 2009. With this value of baseline, the average distance between the two ascending images was 131m. Also, the temporal baseline is taken unrestricted due to the aim of study was to research for the activity of Katouna fault

zone which is a geologically evolutionary phenomenon. The number of the pairs of scenes to produce interferograms was 35. The stacking processing involves the average of coherence component in order to choose a high-quality region as reference. For this reason, an area with coherence value 0.95 is selected.

In order to select the reference point, some criteria for the selection are dictated by the applied method, such as the high quality of the point in terms of phase stability overtime. Others are related to the regional tectonic setting of the area and the related pattern of deformation which needs to be extracted (Parcharidis et al., 2009). The selection of the reference point is very important of the procedure, as the final deformation rates are affected by that selection (Papanikolaou et al., 2010). In this study, the reference point was taken based on the geological stability, which means it was far from the main fault zone of Katouna. Especially, the reference region was taken in the mainland of Greece and to the east, in Pindos area, in an area with a good coherence value. All reference points of all dataset were chosen with the same thought, in the same region.

Thus, for the dataset of interferograms by the all possible pairs of 16 ENVISAT ASAR descending scenes from 2003-2010 with track 322, the perpendicular baseline was 300m, with the average distance between the satellite at the moment of shooting being 142m. The temporal baseline was taken unlimited. The number of interferograms that was created, was 44.

For the other dataset with the 25 ENVISAT ASAR descending scenes from 2003-2010 with track 50, the perpendicular baseline was taken 350m, and the temporal baseline was taken unrestricted. The average distance of perpendicular baseline was 145m and the number of pairs of the scenes which was involved in the interferometric stacking was 100.

On the other hand, for the ERS datasets, 19 ERS-2 ASAR ascending images from 1995-1999, the perpendicular baseline was taken 350m, and the temporal baseline

was taken unrestricted. The average distance of perpendicular baseline was 179m and the number of pairs of the scenes which was involved in the interferometric stacking was 55. Also, for 23 ERS-2 ASAR descending images from 1995-1999, the perpendicular baseline was taken 350m, and the temporal baseline was taken unrestricted. The average distance of perpendicular baseline was 166m and the number of pairs of the scenes which was involved in the interferometric stacking was 100.

The reference point for SVD processing was the same with the Interferometric Stacking technique. For the SVD algorithm, another important element is that the starting point of the calculations was the first image according to its date. Also, it observed that the SVD algorithm influenced the small datasets. So, for the ENVISAT datasets, ascending and descending (track:322) mode, results were obtained with this algorithm. For ERS datasets, no interferograms were produce by applying the SVD, because they were larger datasets than the other datasets. Through linear regression of the deformation timeseries for every point, arises the deformation in meters per years along the direction of Line of Sight (LOS).

The deformation pattern proved to be difficult to identify, though relatively stable areas for reference positioning have been recognized. Low coherence for the majority of single interferograms, mainly due to the land cover type and to a less extend to possible geometric decorrelation, were the main restriction.

After transformation of the interferometric results from range–Doppler coordinates into map geometry (geographic coordinates), point targets were imported in a GIS environment.

Results

In this section, the interferometric stacking for each dataset and the interferograms with applied SVD algorithm for ENVISAT datasets are presented.

The results from the ENVISAT ASAR ascending datasets support an actual land motion over the region of Akarnania block. From Figure 26, it is deduced that the annual average velocities in the range of Line-Of-Sight (LOS) vary between minimum values of -10 m/y and +10 mm/y, respectively. The lower displacement values along the Line-Of-Sight (LOS) are displayed to the western part of the map and the highest displacement values are seen in the eastern part. These values show a motion away to the satellite. In the central area, where the KFZ is located, the values of the displacements vary in both ascending and descending results. Also, it is observed that, the eastern part moves with higher velocity than the western part of the map.

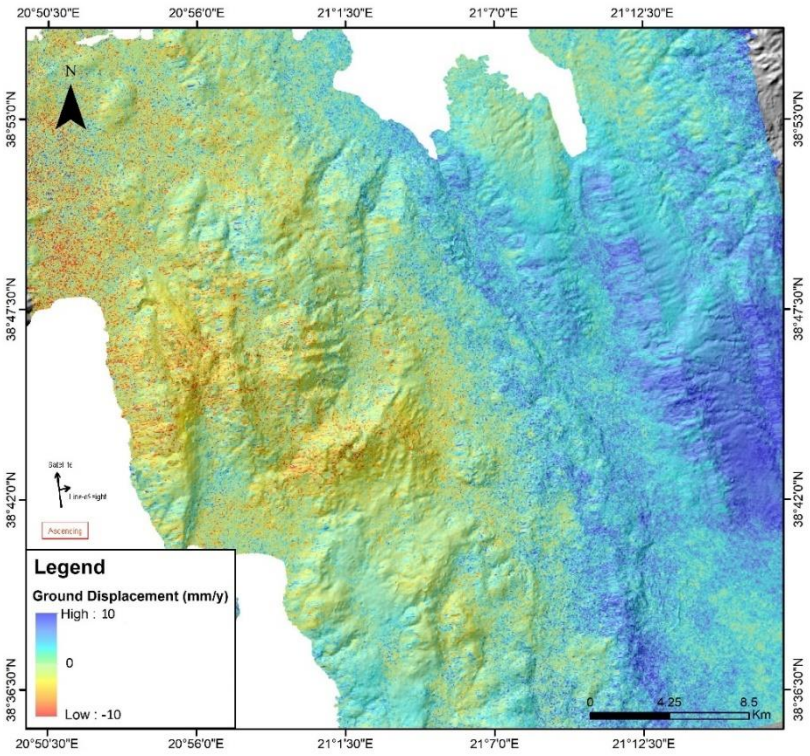

Figure 26 Displacement map produced by Interferometric Stacking, from ascending ENVISAT ASAR images referring to 2002 to 2009 time span

In order to evaluate all the possible interpretations, a frame of descending images away for the main study area is used, for Katouna valley. The aim is to detect this horizontal movement along the KSFZ.

Results from the ENVISAT ASAR descending datasets support an actual land motion over the region of Akarnania block and especially, in the southern part. From Figure 27, it is deduced that the annual average velocities in the range of Line-Of-Sight (LOS) vary between minimum values of -10 m/y and +10 mm/y, respectively. The lower displacement values along the Line-Of-Sight (LOS) are displayed to the eastern part of the map and the highest displacement values appear in the western part. These values show a motion towards to the satellite. Also, it is observed that, the eastern part moves with higher velocity than the western part of the map.

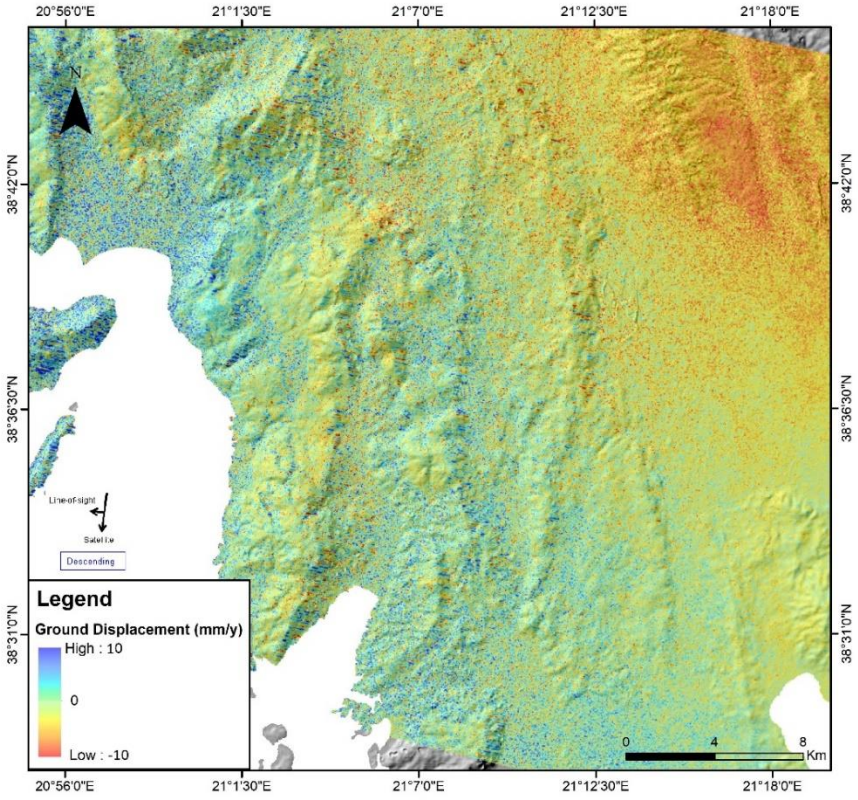

Figure 27 Displacement map produced by Interferometric Stacking, from descending ENVISAT ASAR images referring to 2003 to 2010 time span

Even more interesting are the differences observed in the sign of LOS displacement rates over the study area, which is positive for the descending ENVISAT and negative for the ascending ENVISAT ASAR, (Figure 1 and Figure 2 respectively). This is clearly related to their different acquisition geometries and indicates a significant contribution from horizontal motion, in addition to the vertical component. This is compatible with the field data presented in the previous paragraphs and point to KFZ being probably a left-lateral strike-slip fault. Also, it is very difficult to recognize a discrete line in the transition of the negative to positive displacement. This could be the result of the absence of strong earthquakes with low depths along the fault zone. Another reason for this difficulty could be the presence of the evaporite layer which hosts the fault zone. Synthetic maps correlating the evaporite layer with the transition from negative to positive displacement values in both ascending and descending results are seen below.

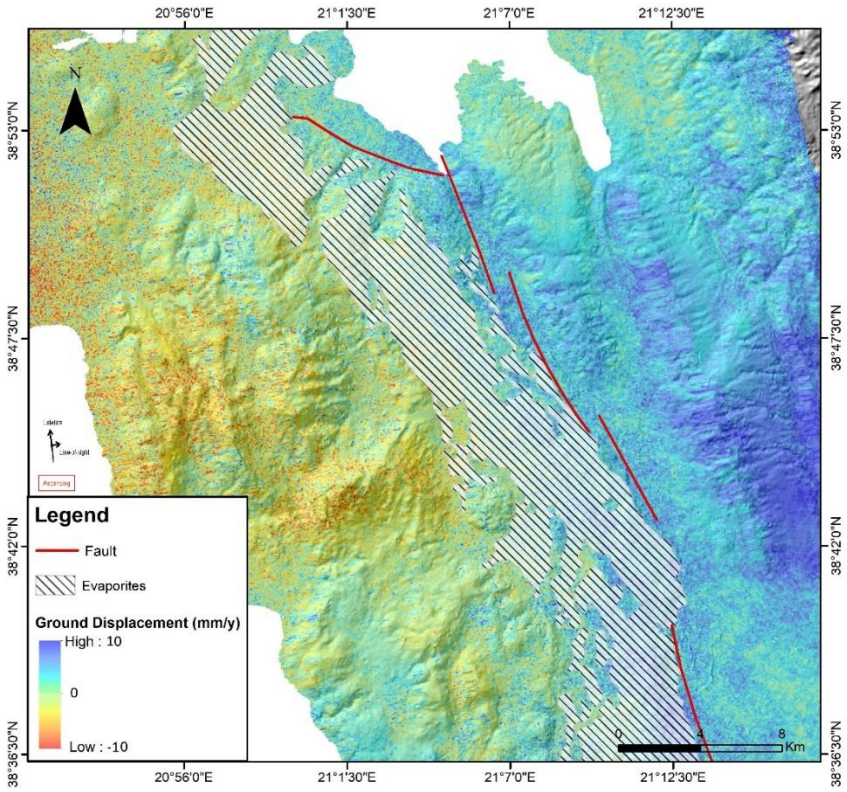

Figure 28 Synthetic map of InSAR result and geological data. Displacement map produced by Interferometric Stacking, from ascending ENVISAT ASAR images referring to 2002 to 2009 time span

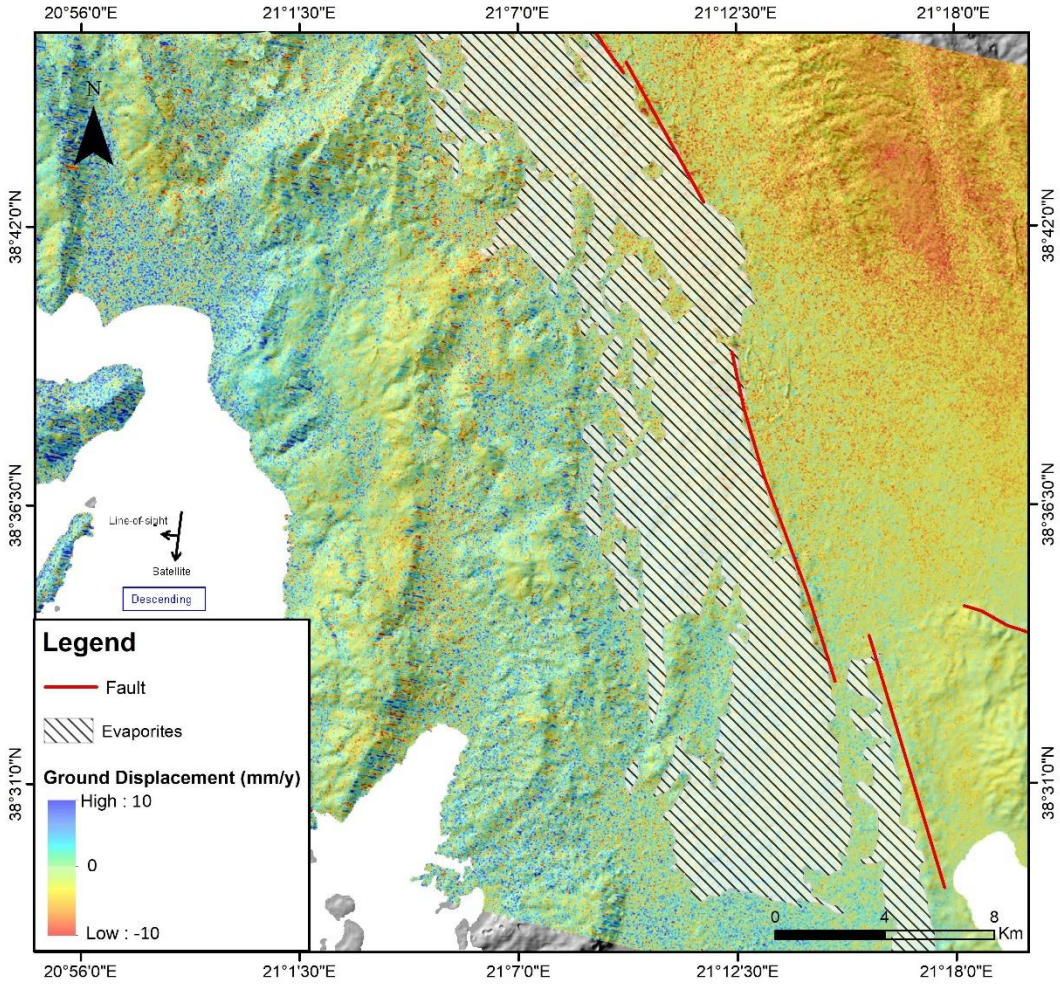

Figure 29 Synthetic map of InSAR result and geological data. Displacement map produced by Interferometric Stacking, from descending ENVISAT ASAR images referring to 2003 to 2010 time span

Furthermore, graphs which display the changing of land motion along the direction E-W, were created. Displacement diagrams, according to the section, over the displacement maps show a smooth transition of positive to negative values in ascending diagram and a smooth transition of negative to positive values in descending diagram. It is possible to detect a very smooth slope trend, which coincides with the area of evaporite layer and the KFZ. This result could confirm the presence of a strike-slip movement along the KFZ.

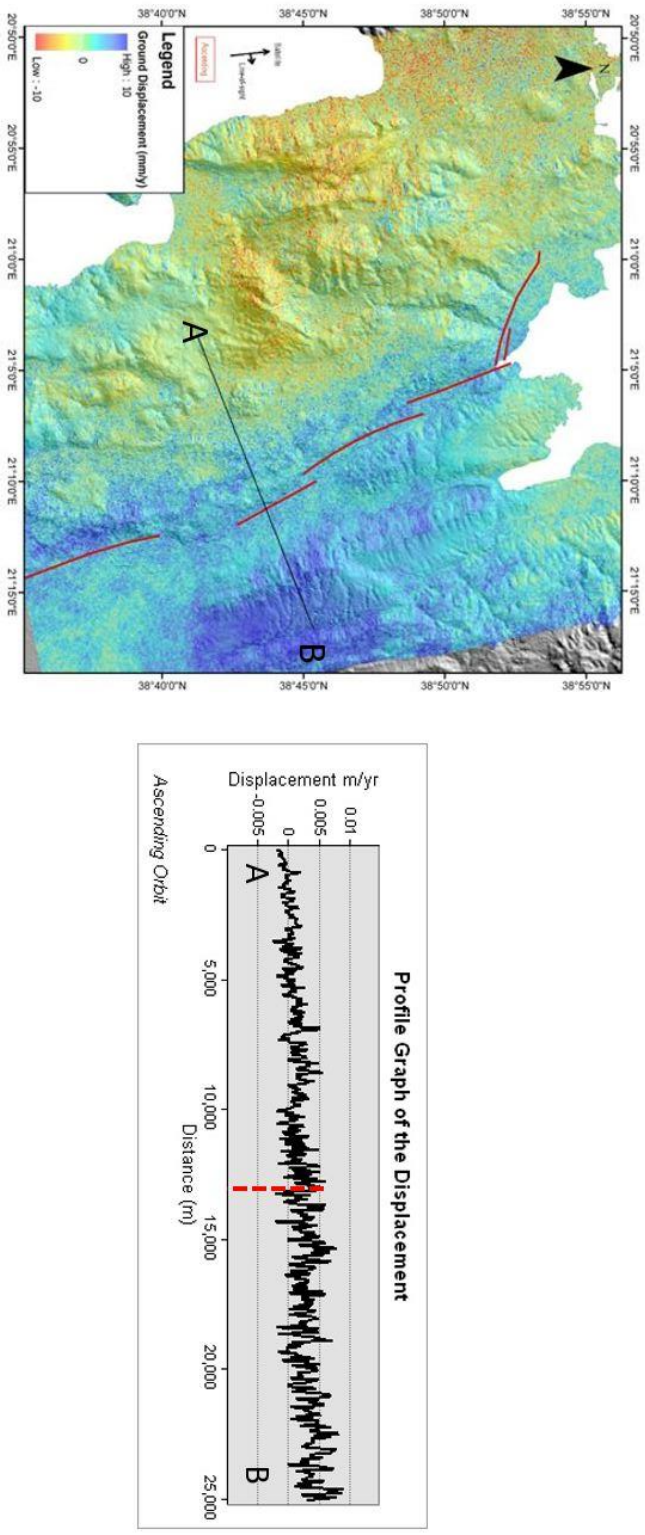

Figure 30 Stacking LOS displacement rate obtained from ascending ENVISAT ASAR images referring to 2002 to 2009 with the main tectonic structures of the area. Section is shown as black line along with their corresponding surface diagrams.

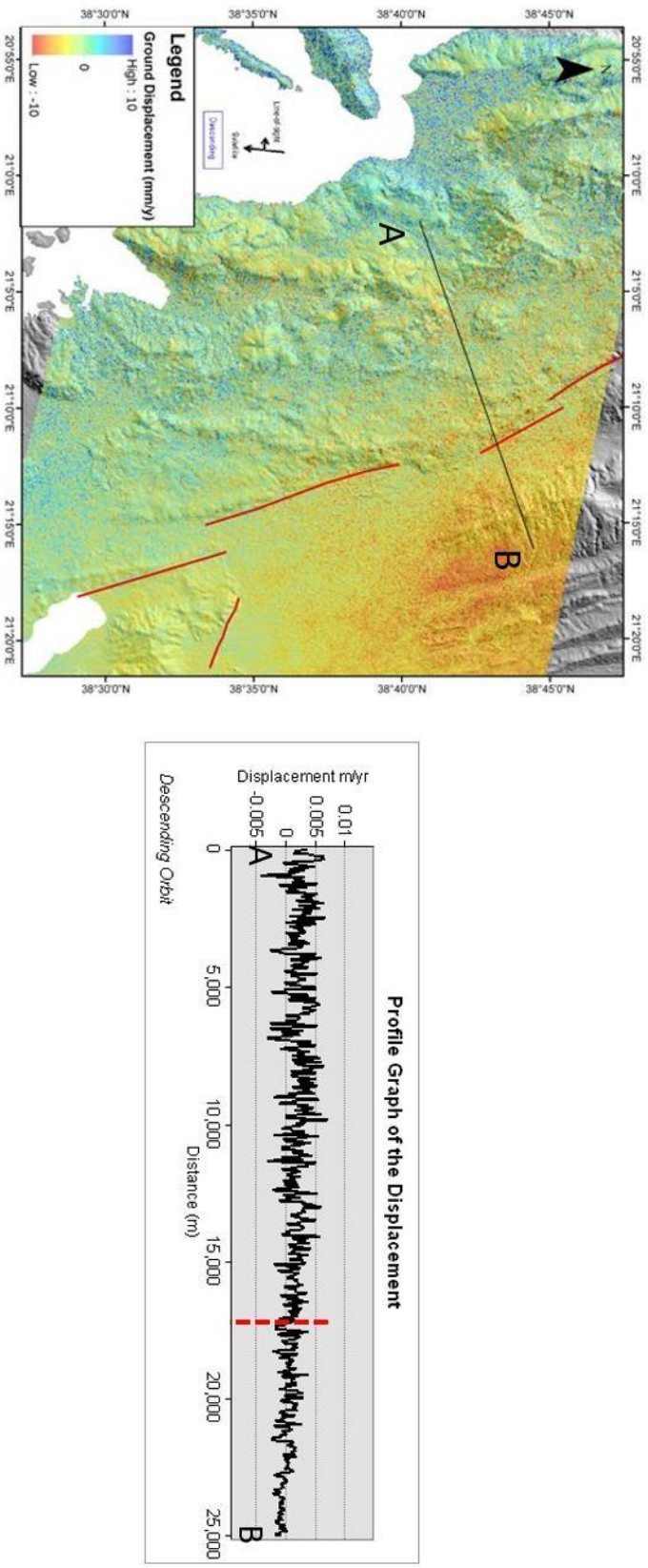

Figure 31 Stacking LOS displacement rate obtained from descending ENVISAT ASAR images referring to 2003 to 2010 with the main tectonic structures of the area. Section is shown as black line along with their corresponding surface diagrams.

The maps below were produced with the SVD algorithm. For the ENVISAT datasets, ascending and descending (track:322) mode, some results were obtained from this algorithm. For ERS datasets, no interferograms were produced by applying the SVD, because these are larger datasets.

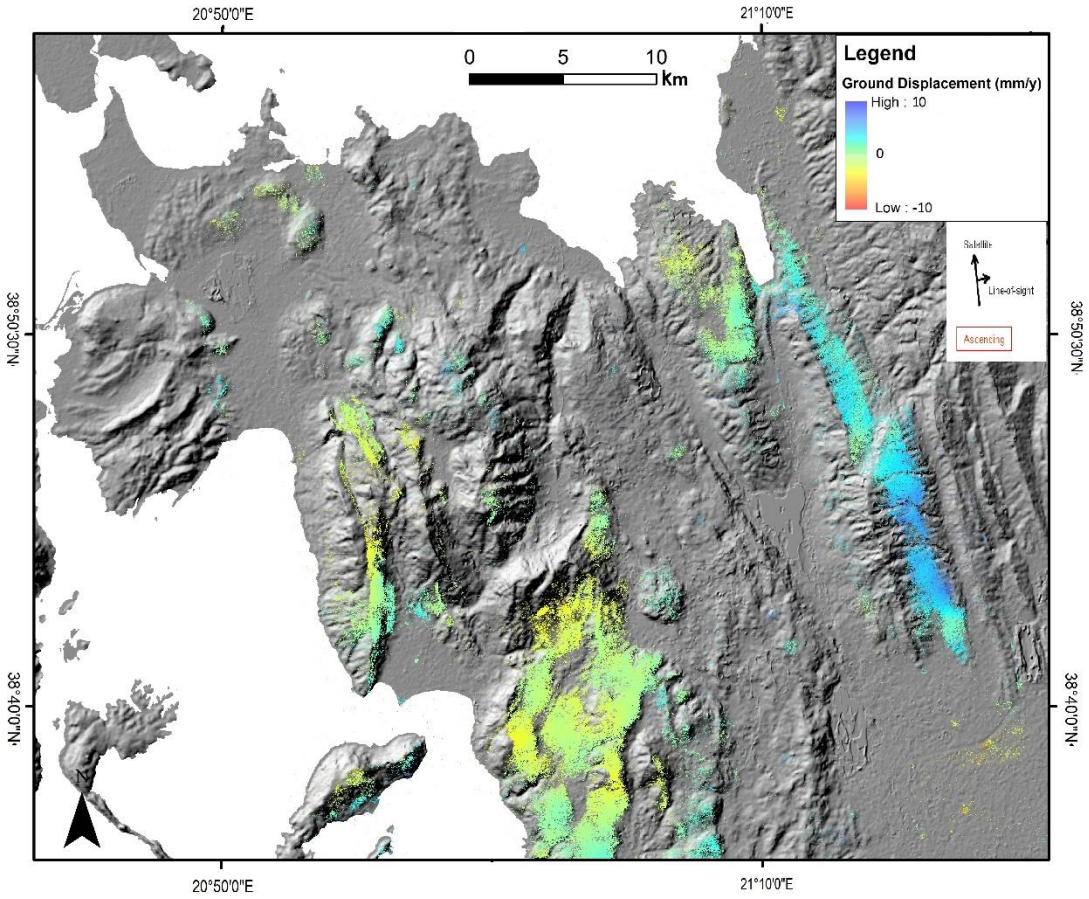

Figure 32 SVD displacement rate from ascending ENVISAT ASAR images referring to 2002 to 2009 time span

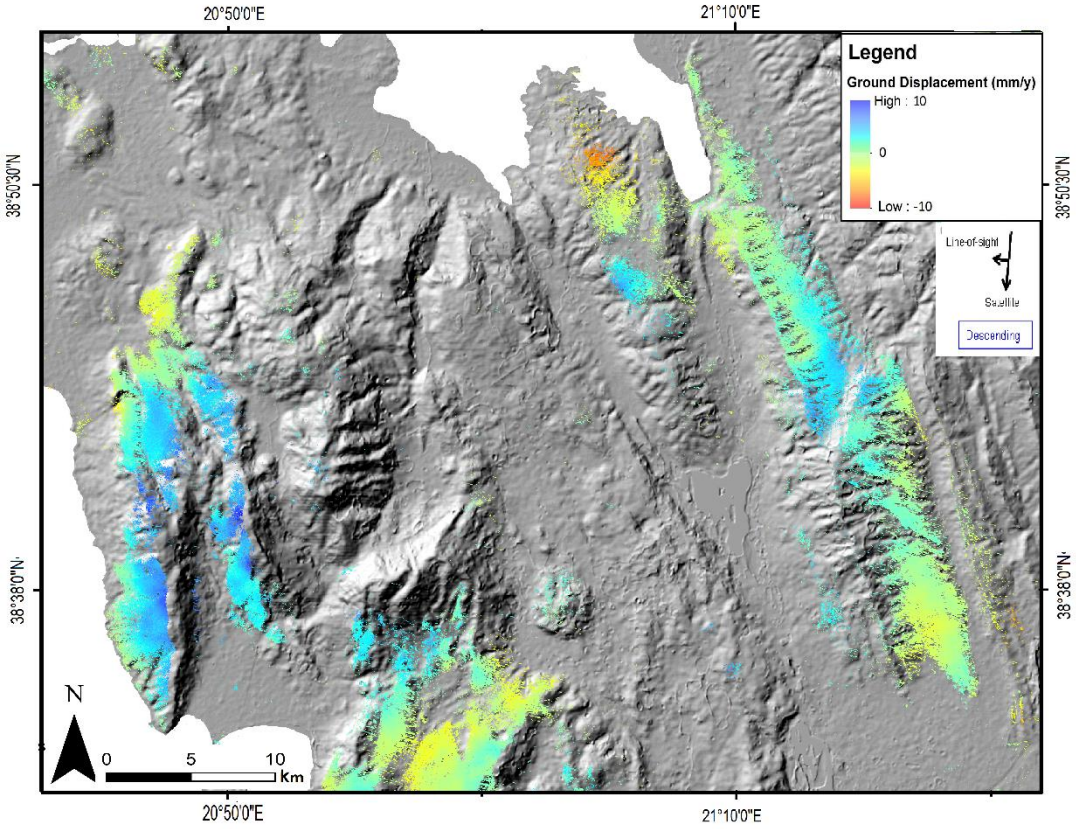

Figure 33 SVD displacement rate from descending ENVISAT ASAR images referring to 2003 to 2010 time span

Discussion

The main objective of the current Master thesis concerns the hypothesis that the KFZ is an active strike-slip fault zone with detected and mapped land motion along the zone. This study consists of two parts. The first part includes the geological observations in the field and the second the detection of land motion by producing multi-temporal interferometric displacement maps, which are then correlated to the geological data. Our results prove that the KFZ is an active left-lateral strike-slip fault, which is crossing through the Aitoloakarnania region and connects the tectonic structures of Amvrakikos Gulf and the Gulf of Patras.

An important finding of this study is the identification of the fault scarps and the related kinematic indicators. This fault zone does not present a single continuous surface but rather consists of several discrete surfaces. This is directly related to the mechanical behavior of the evaporite layer in which the fault zone is hosted. As for the kinematics of the fault zone the main evidence for the type of movement which occurs along comes from the observed slickensides. These show that a strong horizontal component has participated in the overall movement of the fault. The observed shallow plunging slickenlines strike NNW which is also the strike of the fault zone. Furthermore, the kinematic indicators on the slip surfaces correspond to ridge-in-groove lineation which is taking place due to friction between footwall and hanging wall. Based on the above the Katouna Fault Zone and its continuation towards the SSE is possible to transfer fault transfers the movement between two extensional grabens, the graben of Gulf of Amvrakikos and the Gulf of Patras.

Taking a step further, it is possible to characterize this strike-slip fault as a transfer fault. Transfer faults represent strike-slip faults, which transfer the movement between two extensional faults or contractional faults (Fossen, 2016). In our case study, the transfer fault transfers the movement between two extensional

grabens, the graben of Gulf of Amvrakikos and the Gulf of Patras. This fact supports the view that the KFZ is a strike-slip fault.

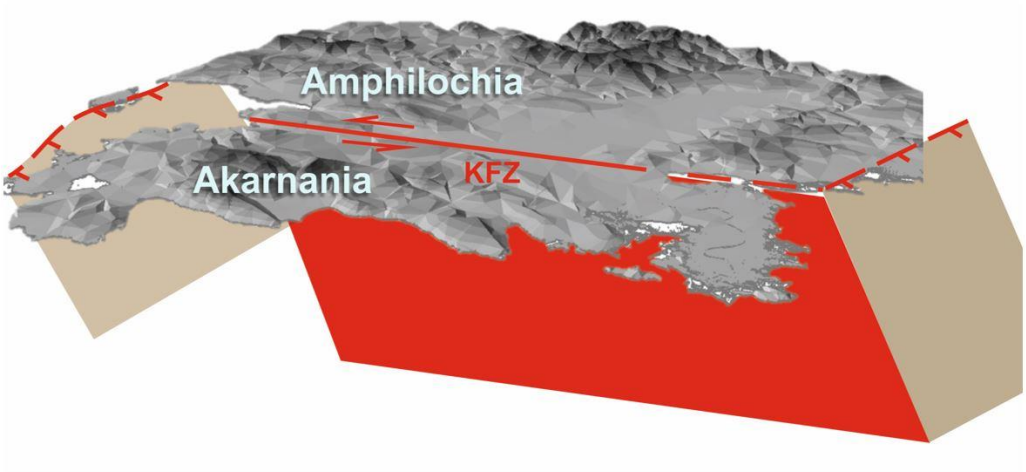

Figure 34 The KFZ as a transfer fault between to grabens

In extensional regimes and especially the releasing bends are ideal locations for reactive diapirism, and the locations where one would expect diapirs to form along strike-slip fault (Fossen, 2016). It is noticeable that this fact supports the hypothesis that the KFZ must be a strike-slip fault. If this is the case, then the fault system is controlled by the Hellenides orogen.

This is further supported by the fact that the GPS vectors show a SW motion but to the west of fault zone the values are higher than to the east of fault zone. That occurs on the north part of the KFZ. This could indicate that the KFZ delimits two different blocks. This result agrees with the hypothesis of Vassilakis et al., 2011, Chousianitis et al., 2015 and Perouse et al., 2016 that the KFZ is a boundary of block. The northern KFZ accommodates the motion relative to continental Greece by active transtension along the Katouna valley. For the direction of vectors and for the values of them, it is suggested that the movement along the KFZ is left-lateral.

Nevertheless, the absence of gradient in the fault-parallel component of velocity GPS vectors across the KFZ is noticeable.

Results from the ENVISAT ASAR descending and ascending datasets support an actual land motion associated with the KFZ, it is deduced that the annual average velocities in the range of Line-Of-Sight (LOS) vary between minimum values of -10

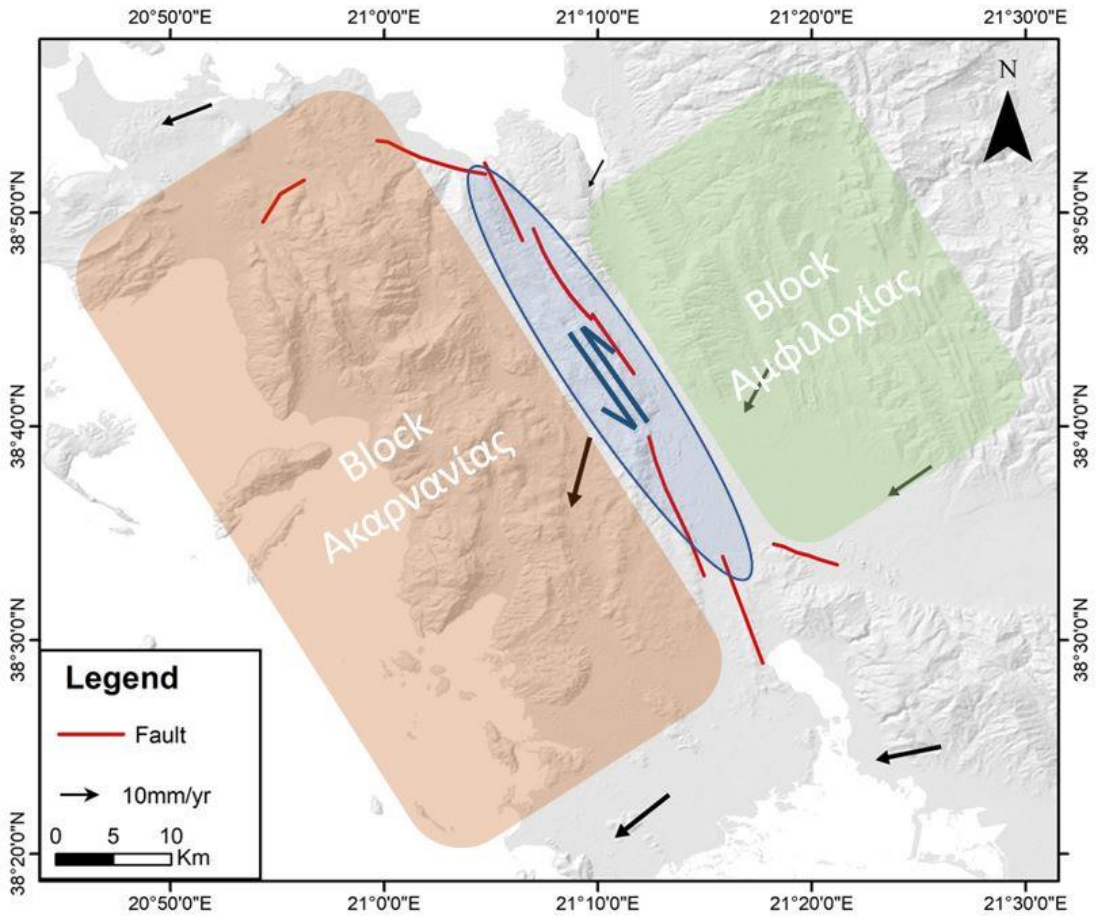

Figure 35 The evidences of left-lateral movement between the two blocks

m/y and +10 mm/y, respectively.

On the other hand, InSAR results show the differential movement across the fault zone. The differences in the sign of LOS displacement rates over the study area which is positive for the descending ENVISAT and negative for the ascending ENVISAT ASAR results are remarkable. This result is clearly related to their different

acquisition geometries and indicates some contribution from horizontal motion in addition to the vertical component.

The boundary between negative to positive displacements is not a discrete line but rather a wide zone of transition. It is remarkable that the boundaries of this zone seem to be identical with the geological boundaries of evaporite layer. This is further evidence indicating that the fault zone geometry and the mechanical behavior of the fault is directly related to the mechanical behavior of the evaporite layer. The zone of transition is a result of the brittle-plastic attitude of evaporite

layer on the surface. According to the geological section, it fits that the location of fault zone is controlled by the evaporite layer.

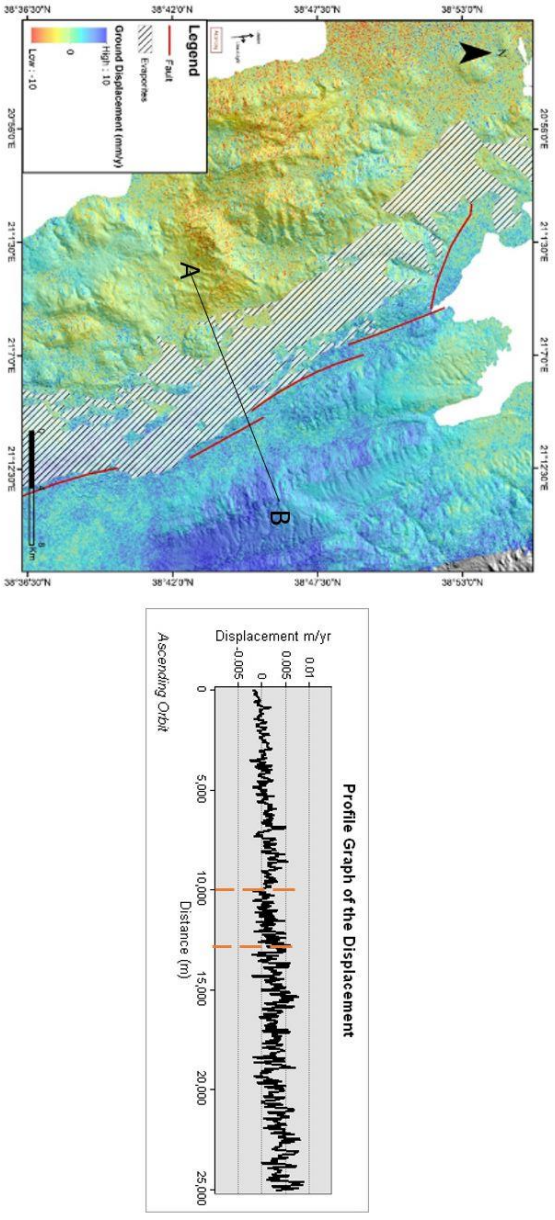

Figure 36 Stacking LOS displacement rate obtained from ascending ENVISAT ASAR images referring to 2002 to 2009 with the main tectonic structures of the area. Section is shown as black line along with their corresponding surface diagrams. Also, in the graph it is located the boundary of evaporite layer.

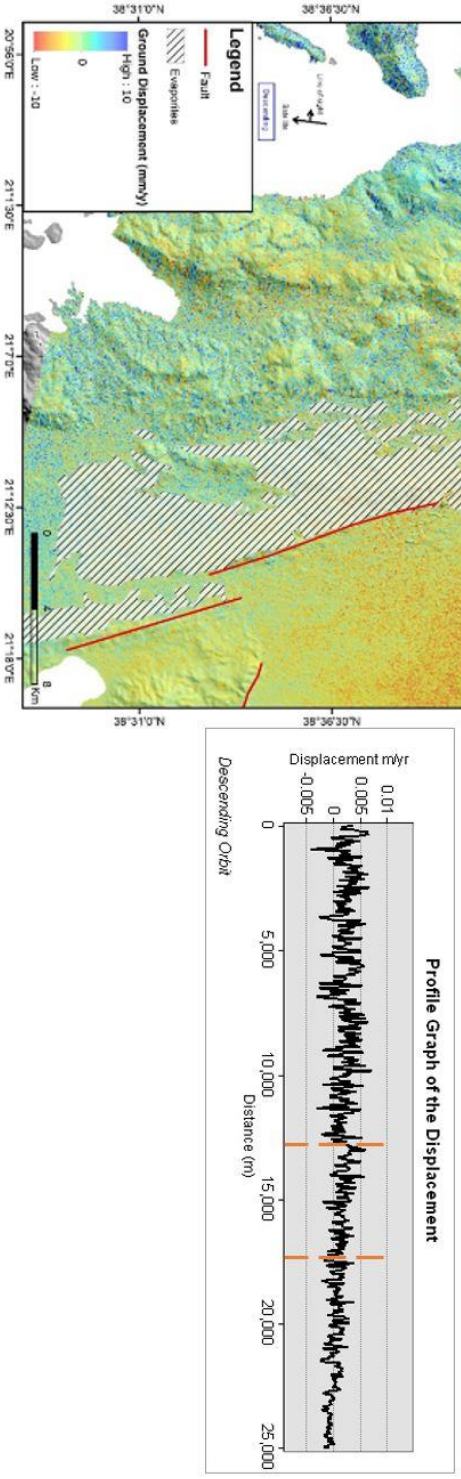

Figure 37Stacking LOS displacement rate obtained from descending ENVISAT ASAR images referring to 2003 to 2010 with the main tectonic structures of the area. Section is shown as black line along with their corresponding surface diagrams. Also, in the graph it is located the boundary of evaporite layer.

It is also significant to point out the correlation of GPS vectors with the InSAR results. This cannot be done in a simple manner because the GPS vectors show the horizontal components and the InSAR results measure the displacement in Line of Sight (LOS). So, the results are correlated well. Also, the values of InSAR results are quite low compared to the values of GPS vector. This could be explained by the fact that the horizontal component is dominant and the InSAR results measure the ground motion in the LOS.

Future research, could include the processing of High resolution radar images such as Terra-SAR-X or/and Sentinel-1, aiming a more efficient approach of the monitoring of the broader area of Katouna valley. Additionally, in the case of monitoring active faults, longer time observation providing a rich data set for processing is necessary in order to obtain accurate and robust results.

Conclusions

The conclusions of the Master thesis are outlined below:

1. The Katouna fault zone is a left-lateral strike slip fault which strikes NNW-SSE with slickensides plunging NW (330^{o}). It is a transfer fault that transfers the movement between two extensional grabens, the graben of Gulf of Amvrakikos and the Gulf of Patras.
2. The northward termination of KFZ is along the ESE-WSW Loutraki fault, which shows a typical morphology of an active normal fault. Loutraki fault does not have a continuous trace and prominent scarp for the same reason with the KFZ because it is hosted by the evaporites. In places this fault cuts through Mesozoic limestones and there the fault plane can be readily observed.
3. Monastiraki fault is a structure away from the main fault zone of the case study. It's a normal fault with a very clear slip surface. On the slip surface, slickensides are parallel to sub-parallel to the dip direction were found.
4. The GPS vectors show a SW motion but to the west of fault zone the values are higher than to the east of fault zone. The northern KFZ accommodates the motion which is related to continental Greece by active transtension along the Katouna valley. For the direction of vectors and for the values of them, it is suggested that the movement along the KFZ could be left-lateral.
5. InSAR results show the differential movement across the fault zone. This result is clearly related to their different acquisition geometries and indicates some contribution from horizontal motion in addition to the vertical component.
6. The transition of the negative to positive displacements isn't a discrete line but a zone of transition. It is remarkable that the boundaries of this zone seem to be identical with the geological boundaries of evaporite layer. This evidence could indicate that the fault zone is controlled by the evaporite layer.

References

Anastasakis, G., Piper, D. J., & Tziavos, C. (2007). Sedimentological response to neotectonics and sea-level change in a delta-fed, complex graben: Gulf of Amvrakikos, western Greece. *Marine Geology*, *236*(1), 27-44.

Avery, T. E., & Berlin, G. L. (1992). Fundamentals of remote sensing and airphoto interpretation.

Avallone, A., Briole, P., Agatza-Balodimou, A. M., Billiris, H., Charade, O., Mitsakaki, C., ... & Veis, G. (2004). Analysis of eleven years of deformation measured by GPS in the Corinth Rift Laboratory area. *Comptes Rendus Geoscience*, *336*(4), 301-311.

Baker, C., Hatzfeld, D. L., Lyon-Caen, H., Papadimitriou, E., & Rigo, A. (1997). Earthquake mechanisms of the Adriatic Sea and Western Greece: implications for the oceanic subduction-continental collision transition. *Geophysical Journal International*, *131*(3), 559-594.

Banerjee, S., & Rao, W. (2017, January). A local reconfiguration based scalable fault tolerant many-processor array. In *Design Automation Conference (ASP-DAC), 2017 22nd Asia and South Pacific* (pp. 432-437). IEEE.

Bennett, R. A., Hreinsdóttir, S., Buble, G., Bašić, T., Bačić, Ž., Marjanović, M., ... & Cowan, D. (2008). Eocene to present subduction of southern Adria mantle lithosphere beneath the Dinarides. *Geology*, *36*(1), 3-6.

Berardino, P., Fornaro, G., Lanari, R., & Sansosti, E. (2002). A new algorithm for surface deformation monitoring based on small baseline differential SAR interferograms. *IEEE Transactions on Geoscience and Remote Sensing*, *40*(11), 2375-2383.

Burchfiel, C. B., Nakov, R., Tzankov, T., & Royden, L. H. (2000). Cenozoic extension in Bulgaria and northern Greece: the northern part of the Aegean extensional regime. *Geological Society, London, Special Publications*, *173*(1), 325-352.

Brooks, M., Clews, J. E., Melis, N. S., & Underhill, J. R. (1988). Structural development of Neogene basins in western Greece. *Basin Research*, *1*(3), 129-138.

Bouraoui, S. (2013). *Time series analysis of SAR images using persistent scatterer (PS), small baseline (SB) and merged approaches in regions with small surface deformation* (Doctoral dissertation, Université de Strasbourg).

Clark, C. D., Garrod, S. M., & Pearson, M. P. (1998). Landscape archaeology and remote sensing in southern Madagascar. *International Journal of Remote Sensing*, *19*(8), 1461-1477.

CLEWS, J. E. (1989). Structural controls on basin evolution: Neogene to Quaternary of the Ionian zone, Western Greece. *Journal of the Geological Society*, *146*(3), 447-457.

Cocard, M., Kahle, H. G., Peter, Y., Geiger, A., Veis, G., Felekis, S., ... & Billiris, H. (1999). New constraints on the rapid crustal motion of the Aegean region: recent results inferred from GPS measurements (1993–1998) across the West Hellenic Arc, Greece. *Earth and Planetary Science Letters*, *172*(1), 39-47.

Chamot-Rooke, N., Rangin, C., & Le Pichon, X. (2005). DOTMED—Deep Offshore Tectonics of the Mediterranean: A synthesis of deep marine data in eastern Mediterranean. Mem. Soc. Geol. Fr, 177, 1-64.

Chousianitis, K., Ganas, A., & Evangelidis, C. P. (2015). Strain and rotation rate patterns of mainland Greece from continuous GPS data and comparison between seismic and geodetic moment release. *Journal of Geophysical Research: Solid Earth*, *120*(5), 3909-3931.

Colesanti, C., Ferretti, A., Prati, C., & Rocca, F. (2003). Monitoring landslides and tectonic motions with the Permanent Scatterers Technique. *Engineering Geology*, *68*(1), 3-14.

Colesanti, C., Ferretti, A., Novali, F., Prati, C., & Rocca, F. (2003). SAR monitoring of progressive and seasonal ground deformation using the permanent scatterers technique. *IEEE Transactions on Geoscience and Remote Sensing*, *41*(7), 1685-1701.

Doutsos, T., Kontopoulos, N., & Frydas, D. (1987). Neotectonic evolution of northwestern-continental Greece. *Geologische Rundschau*, *76*(2), 433-450.

Drury, S.A., 1987. Image Interpretation in Geology. Allen & Unwin, London.

Ers Satellite radar vision 2011, August 17. Retrieved from http://www.esa.int/Our_Activities/Observing_the_Earth/ERS_overview

Envisat Satellite radar vision 2012. Retrieved from http://www.esa.int/Our_Activities/Observing_the_Earth/Envisat/Mission_overview

EOLi Platform 2017, May. Retrieved from https://earth.esa.int/web/guest/eoli

Ferretti, A. (2014). Satellite InSAR data: reservoir monitoring from space. EAGE Publications.

Ferretti, A., Prati, C., & Rocca, F. (2001). Permanent scatterers in SAR interferometry. *IEEE Transactions on geoscience and remote sensing*, *39*(1), 8-20.

Ferretti, A., Fumagalli, A., Novali, F., De Zan, F., Rucci, A., & Tebaldini, S. (2014). *U.S. Patent No. 8,711,029*. Washington, DC: U.S. Patent and Trademark Office.

Ferretti, A., Savio, G., Barzaghi, R., Borghi, A., Musazzi, S., Novali, F., ... & Rocca, F. (2007). Submillimeter accuracy of InSAR time series: Experimental validation. *IEEE Transactions on Geoscience and Remote Sensing*, *45*(5), 1142-1153.

Fletcher, K. European Space Agency, European Space Research and Technology Centre, ESTEC (2007) InSAR principles: guidelines for SAR interferometry processing and interpretation.

Ford, D., & Williams, P. D. (2013). *Karst hydrogeology and geomorphology*. John Wiley & Sons.

Fossen, H. (2016). Structural geology. Cambridge University Press.

Fujiwara, S., Yarai, H., Ozawa, S., Tobita, M., Murakami, M., Nakagawa, H., ... & Werner, C. L. (1998). Surface displacement of the March 26, 1997 Kagoshima-Ken-Hokuseibu Earthquake in Japan from synthetic aperture radar interferometry. *Geophysical research letters*, *25*(24), 4541-4544.

Gabriel, A. K., Goldstein, R. M., & Zebker, H. A. (1989). Mapping small elevation changes over large areas: differential radar interferometry. Journal of Geophysical Research: Solid Earth, 94(B7), 9183-9191.

Ganas, A., Serpelloni, E., Drakatos, G., Kolligri, M., Adamis, I., Tsimi, C., & Batsi, E. (2009). The Mw 6.4 SW-Achaia (western Greece) earthquake of 8 June 2008: Seismological, field, GPS observations, and stress modeling. *Journal of Earthquake Engineering*, *13*(8), 1101-1124.

GAMMA Remote Sensing Software 2000-2017. Retrieved from https://www.gamma-rs.ch/

Gkardi, E., (2011) Tectonic Analysis of the fault zones of Amfilophia and Katouna (Master thesis, University of Patras, Department of Geology)

Goldstein, R. (1995). Atmospheric limitations to repeat-track radar interferometry. *Geophysical research letters*, *22*(18), 2517-2520.

GPS Global Positioning System 2017, June 6. Retrieved from http://www.gps.gov/systems/gps/

GLONASS Information Analytical Centre of GLONASS and GPS Controlling, 2005-2017. Retrieved from https://www.glonass-iac.ru/en/

Haslinger, F., Kissling, E., Ansorge, J., Hatzfeld, D., Papadimitriou, E., Karakostas, V., ... & Peter, Y. (1999). 3D crustal structure from local earthquake tomography around the Gulf of Arta (Ionian region, NW Greece). *Tectonophysics*, *304*(3), 201-218.

Hatzfeld, D., Kassaras, I., Panagiotopoulos, D., Amorese, D., Makropoulos, K., Karakaisis, G., & Coutant, O. (1995). Microseimicity and strain pattern in northwestern Greece. *Tectonics*, *14*(4), 773-785.

Hanssen, R. F. (2001). *Radar interferometry: data interpretation and error analysis* (Vol. 2). Springer Science & Business Media.

Hanssen, R. F., Feijt, A. J., & Klees, R. (2001). Comparison of Precipitable Water Vapor Observations by Spaceborne Radar Interferometry and Meteosat 6.7-μ m Radiometry. *Journal of Atmospheric and Oceanic Technology*, *18*(5), 756-764.

Hollenstein, C., Müller, M. D., Geiger, A., & Kahle, H. G. (2008). Crustal motion and deformation in Greece from a decade of GPS measurements, 1993–2003. *Tectonophysics*, *449*(1), 17-40.

Jolivet, L., & Brun, J. P. (2010). Cenozoic geodynamic evolution of the Aegean. *International Journal of Earth Sciences*, *99*(1), 109-138.

Kahle, H. G., Müller, M. V., Geiger, A., Danuser, G., Mueller, S., Veis, G., ... & Paradissis, D. (1995). The strain field in northwestern Greece and the Ionian Islands: results inferred from GPS measurements. *Tectonophysics*, *249*(1-2), 41-52.

Konstantinou, K. I., Evangelidis, C. P., & Melis, N. S. (2011). The 8 June 2008 Mw 6.4 earthquake in Northwest Peloponnese, Western Greece: a case of fault reactivation in an overpressured lower crust? *Bulletin of the Seismological Society of America*, *101*(1), 438-445.

Le Pichon, X., & Angelier, J. (1979). The Hellenic arc and trench system: a key to the neotectonic evolution of the eastern Mediterranean area. *Tectonophysics*, *60*(1), 1-42.

Le Pichon, X., Angelier, J., Aubouin, J., Lyberis, N., Monti, S., Renard, V., ... & Matthews, D. (1979). From subduction to transform motion: a seabeam survey of the Hellenic trench system. *Earth and Planetary Science Letters*, *44*(3), 441-450.

Louvari, E., Kiratzi, A. A., & Papazachos, B. C. (1999). The Cephalonia transform fault and its extension to western Lefkada Island (Greece). *Tectonophysics*, *308*(1), 223-236.

Louvari, E. K. (1998). Fault plane solutions in the Aegean Sea and the surrounding area and their tectonic implication. *Boll. Geof. Teor. Appl*, *39*(3), 199-218.

Le Pichon, X., Chamot-Rooke, N., Lallemant, S., Noomen, R., & Veis, G. (1995). Geodetic determination of the kinematics of central Greece with respect to Europe: Implications for eastern Mediterranean tectonics. *Journal of Geophysical Research: Solid Earth*, *100*(B7), 12675-12690.

McKenzie, D. (1972). Active tectonics of the Mediterranean region. *Geophysical Journal International*, *30*(2), 109-185.

McKenzie, D. (1978). Active tectonics of the Alpine—Himalayan belt: the Aegean Sea and surrounding regions. *Geophysical Journal International*, *55*(1), 217-254.

McKenzie, D., & Jackson, J. (1983). The relationship between strain rates, crustal thickening, palaeomagnetism, finite strain and fault movements within a deforming zone. *Earth and Planetary Science Letters*, *65*(1), 182-202.

Melis, N. S., & Burton, P. W. (1988, March). Seismicity and crustal deformation in regions of central Greece. In *GEOPHYSICAL JOURNAL-OXFORD* (Vol. 92, No. 3, pp. 529-529). OSNEY MEAD, OXFORD, OXON, ENGLAND OX2 0EL: BLACKWELL SCIENCE LTD.

Mercier, J. L., Sorel, D., Vergely, P., & Simeakis, K. (1989). Extensional tectonic regimes in the Aegean basins during the Cenozoic. *Basin research*, *2*(1), 49-71.

Massonnet, D., & Feigl, K. L. (1998). Radar interferometry and its application to changes in the Earth's surface. Reviews of geophysics, 36(4), 441-500.

Natural Resources Canada, 2016, November 27, Retrieved from http://www.nrcan.gc.ca.

Osmanoğlu, B., Sunar, F., Wdowinski, S., & Cabral-Cano, E. (2016). Time series analysis of InSAR data: Methods and trends. *ISPRS Journal of Photogrammetry and Remote Sensing*, *115*, 90-102.

Papazachos, B. C., Karakostas, V. G., Papazachos, C. B., & Scordilis, E. M. (2000). The geometry of the Wadati–Benioff zone and lithospheric kinematics in the Hellenic arc. *Tectonophysics*, *319*(4), 275-300.

Perouse, E., Chamot-Rooke, N., Rabaute, A., Briole, P., Jouanne, F., Georgiev, I., & Dimitrov, D. (2012). Bridging onshore and offshore present-day kinematics of central and eastern Mediterranean: implications for crustal dynamics and mantle flow. *Geochemistry, Geophysics, Geosystems*, *13*(9).

Pérouse, E., Sébrier, M., Braucher, R., Chamot-Rooke, N., Bourlès, D., Briole, P., ... & Arsenikos, S. (2017). Transition from collision to subduction in Western Greece: the

Katouna–Stamna active fault system and regional kinematics. *International Journal of Earth Sciences*, *106*(3), 967-989.

Papanikolaou, D. (2013). Tectonostratigraphic models of the Alpine terranes and subduction history of the Hellenides. *Tectonophysics*, *595*, 1-24.

Papapetrou-Zamanis, A., (1969). Le lac de Vouliagmeni (Attiki). Ann. Geol. Pays Hell. 21, 210–216

Pérouse, E. (2013). *Cinématique et tectonique active de l'Ouest de la Grèce dans le cadre géodynamique de la Méditerranée Centrale et Orientale* (Doctoral dissertation, Université Paris Sud-Paris XI).

Parcharidis I., 2016. Principles of Remote Sensing. (in greek).

Papanikolaou D., 2015. Geology of Greece, Athens, Greece: Patakis Publications.

Parcharidis, I., Foumelis, M., Kourkouli, P., & Wegmuller, U. (2009). Persistent Scatterers InSAR to detect ground deformation over Rio-Antirio area (Western Greece) for the period 1992–2000. *Journal of Applied Geophysics*, *68*(3), 348-355.

Papanikolaou, I. D., Foumelis, M., Parcharidis, I., Lekkas, E. L., & Fountoulis, I. G. (2010). Deformation pattern of the 6 and 7 April 2009, MW= 6.3 and MW= 5.6 earthquakes in L'Aquila (Central Italy) revealed by ground and space based observations. Natural Hazards and Earth System Sciences, 10(1), 73.

Picha, F. J. (2002). Late orogenic strike-slip faulting and escape tectonics in frontal Dinarides-Hellenides, Croatia, Yugoslavia, Albania, and Greece. *AAPG bulletin*, *86*(9), 1659-1671.

Rosenbaum, G., & Lister, G. S. (2004). Neogene and Quaternary rollback evolution of the Tyrrhenian Sea, the Apennines, and the Sicilian Maghrebides. *Tectonics*, *23*(1).

Reilinger, R., McClusky, S., Vernant, P., Lawrence, S., Ergintav, S., Cakmak, R., ... & Nadariya, M. (2006). GPS constraints on continental deformation in the Africa-Arabia-Eurasia continental collision zone and implications for the dynamics of plate interactions. *Journal of Geophysical Research: Solid Earth*, *111*(B5).

Royden, L. H., & Papanikolaou, D. J. (2011). Slab segmentation and late Cenozoic disruption of the Hellenic arc. *Geochemistry, Geophysics, Geosystems*, *12*(3).

Reilinger, R., McClusky, S., Paradissis, D., Ergintav, S., & Vernant, P. (2010). Geodetic constraints on the tectonic evolution of the Aegean region and strain accumulation along the Hellenic subduction zone. *Tectonophysics*, *488*(1), 22-30.

Strozzi, T., Wegmuller, U., Tosi, L., Bitelli, G., & Spreckels, V. (2001). Land subsidence monitoring with differential SAR interferometry. *Photogrammetric engineering and remote sensing*, *67*(11), 1261-1270.

Sandwell, D. T., & Price, E. J. (1998). Phase gradient approach to stacking interferograms. *Journal of Geophysical Research: Solid Earth*, *103*(B12), 30183-30204.

Scharroo, R., & Visser, P. (1998). Precise orbit determination and gravity field improvement for the ERS satellites. *Journal of Geophysical Research: Oceans*, *103*(C4), 8113-8127.

Tarayre, H., & Massonnet, D. (1996). Atmospheric Propagation heterogeneities revealed by ERS-1 interferometry. *Geophysical Research Letters*, *23*(9), 989-992.

Touzi, R., Lopes, A., Bruniquel, J., & Vachon, P. W. (1999). Coherence estimation for SAR imagery. *IEEE Transactions on Geoscience and Remote Sensing*, *37*(1), 135-149.

Underhill, J. R. (1989). Late Cenozoic deformation of the Hellenide foreland, western Greece. *Geological Society of America Bulletin*, *101*(5), 613-634.

Usai, S. (2003). A least squares database approach for SAR interferometric data. *IEEE Transactions on Geoscience and Remote Sensing*, *41*(4), 753-760.

Vassilakis, E., Royden, L., & Papanikolaou, D. (2011). Kinematic links between subduction along the Hellenic trench and extension in the Gulf of Corinth, Greece: a multidisciplinary analysis. *Earth and Planetary Science Letters*, *303*(1), 108-120.

Valkaniotis, S., Ganas, A., Papathanassiou, G., & Papanikolaou, M. (2014). Field observations of geological effects triggered by the January–February 2014 Cephalonia (Ionian Sea, Greece) earthquakes. *Tectonophysics*, *630*, 150-157.

Vassilakis, E., Royden, L., & Papanikolaou, D. (2006, October). Extensional neotectonic structures adjacent and sub-parallel to the Hellenic trench. In *Geological Society of America Abstracts with Programs* (Vol. 38, No. 7, p. 549).

Vlachou, 2006 Βλάχου Κ., 2006. GPS Μετρήσεις Στην Ευρύτερη Περιοχή Πατραϊκού Κόλπου. Τομέας Γεωφυσικής - Γεωθερμίας, Τμήμα Γεωλογίας και Γεωπεριβάλλοντος, Εθνικό και Καποδιστριακό Πανεπιστήμιο Αθηνών, Αθήναι, σελ.159.

Wegmuller, U., Werner, C., & Strozzi, T. (1998, July). SAR interferometric and differential interferometric processing chain. In *Geoscience and Remote Sensing Symposium Proceedings, 1998. IGARSS'98. 1998 IEEE International*(Vol. 2, pp. 1106-1108). IEEE.

Wasowski, J., & Bovenga, F. (2014). Investigating landslides and unstable slopes with satellite Multi Temporal Interferometry: Current issues and future perspectives. Engineering Geology, 174, 103-138.

Zebker, H. A., Rosen, P. A., & Hensley, S. (1997). Atmospheric effects in interferometric synthetic aperture radar surface deformation and topographic maps. *Journal of geophysical research: solid earth*, *102*(B4), 7547-7563.